

THESIS FOR THE DEGREE OF LICENCIATE OF ENGINEERING

# **Nanoplasmonic Sensing of Materials for Energy Applications**

FERRY ANGGORO ARDY NUGROHO



## **CHALMERS**

Department of Physics  
CHALMERS UNIVERSITY OF TECHNOLOGY  
Gothenburg, Sweden 2016

Nanoplasmonic Sensing of Materials for Energy Applications  
FERRY ANGGORO ARDY NUGROHO

© FERRY ANGGORO ARDY NUGROHO, 2016

Department of Physics  
Chalmers University of Technology  
SE-412 96 Gothenburg  
Sweden  
Telephone + 46 (0)31-772 3007

Cover: A cartoon representation of the concept of a nanoplasmonic sensing. Idea by the Author and illustration by Nesia Anindita from Heimlo Studio ([be.net/heimlo](http://be.net/heimlo))

Printed at Chalmers Reproservice  
Gothenburg, Sweden 2016

Ferry Anggoro Ardy Nugroho  
Department of Physics  
Chalmers University of Technology

## Abstract

Sensors are omnipresent in our daily life. They are used in many applications ranging from the touch screen in our smartphones to more critical contexts such as pollution monitoring. Although sensors have been developed for a long time, the demands are continuously increasing and many sensors still suffer from insufficient selectivity and/or sensitivity. The development of nanosensors has been suggested as one solution to push sensor performance boundaries further by exploiting the unique phenomena occurring at the nanoscale. One of the nanotechnology subareas of particular interest for sensing applications is nanoplasmonics, which explores the localized surface plasmon resonance (LSPR) phenomenon occurring in metal nanoparticles.

In this thesis, nanoplasmonic sensing is developed and utilized in the context of the current challenges in the energy and environmental fields, or more specifically, the hydrogen economy, Carbon Capture and Storage (CCS) and solar energy harvesting technologies.

In the first part, *direct* nanoplasmonic sensing based on AuPd alloy nanoparticles is explored for use as next-generation hydrogen sensors. To facilitate the nanofabrication of such alloy nanostructures, a bottom-up nanofabrication strategy for producing supported alloy nanoparticles with excellent control of their composition is developed. The performance of the fabricated AuPd alloy hydrogen sensors is then assessed and favorably compared to the performance targets set for hydrogen sensors to be used in fuel cell vehicles.

In the second part, *indirect* nanoplasmonic sensing is established as an analytical tool to assess key properties of energy related materials for CCS and organic photovoltaics. The first study constitutes an investigation of CO<sub>2</sub> adsorption in a microporous polymer, and the optical determination of the CO<sub>2</sub> isosteric heat of adsorption. The second study addresses the thickness dependence of the glass transition temperature of a polymer:fullerene blend used as light absorber layer in organic photovoltaic devices. These two studies establish indirect nanoplasmonic sensing as a reliable and important analytical tool for the quantitative assessment of material properties of systems highly relevant for energy applications.

**Keywords:** sensors, localized surface plasmon resonance, plasmonic sensors, indirect nanoplasmonic sensing, nanofabrication, palladium, alloy nanoparticles, hydrogen sensors, carbon capture and storage, microporous polymers, PIM-1, adsorption, glass transition temperature, organic photovoltaics, polymer:fullerene blends, film thickness dependence

## LIST OF APPENDED PAPERS

This thesis is based on the work presented in the following publications:

### **Paper I**

*Bottom-Up Nanofabrication of Supported Noble Metal Alloy Nanoparticle Arrays for Plasmonics*

Ferry A. A. Nugroho, Beniamino Iandolo, Jakob B. Wagner and Christoph Langhammer

Submitted for publication

### **Paper II**

*Hysteresis-Free Nanoplasmonic Pd–Au Alloy Hydrogen Sensors*

Carl Wadell<sup>‡</sup>, Ferry A. A. Nugroho<sup>‡</sup>, Emil Lidström, Beniamino Iandolo, Jakob B. Wagner and Christoph Langhammer

(<sup>‡</sup>equal contribution)

Nano Letters, **15** (5), 3563–3570 (2015)

### **Paper III**

*UV–Visible and Plasmonic Spectroscopy of the CO<sub>2</sub> Adsorption Energetics in a Microporous Polymer*

Ferry A. A. Nugroho, Chao Xu, Niklas Hedin and Christoph Langhammer

Analytical Chemistry, **87** (20), 10161–10165 (2015)

### **Paper IV**

*Plasmonic Nanospectroscopy Sheds Light on the Thermal Stability of a Polymer Solar Cell Blend*

Ferry A. A. Nugroho, Camilla Lindqvist, Amaia Diaz de Zerio Mendaza, Christian Müller and Christoph Langhammer

Submitted for publication

## RELATED PAPER NOT INCLUDED IN THIS THESIS

*Hydride Formation Thermodynamics and Hysteresis in Individual Pd Nanocrystals with Different Size and Shape*

Svetlana Syrenova, Carl Wadell, Ferry A. A. Nugroho, Tina A. Gschneidner, Yuri A. Diaz Fernandez, Giammarco Nalin, Dominika Świtlik, Fredrik Westerlund, Tomasz J. Antosiewicz, Vladimir P. Zhdanov, Kasper Moth-Poulsen and Christoph Langhammer

Nature Materials, **14** (12), 1236–1244 (2015)

## PATENT APPLICATION

*Surface Plasmon Resonance Gas Sensor, Gas Sensing System, and Gas Sensing Method*

Bengt Kasemo, Christoph Langhammer and Ferry A. A. Nugroho

PCT/EP2014/078484, publication number WO2015091811 A1

## MY CONTRIBUTIONS TO THE APPENDED PAPERS

**Paper I** : Fabricated all samples and performed the optical characterization. Wrote the first draft of the paper.

**Paper II** : Fabricated all samples and performed all the measurements. Analyzed the data and prepared the figures for the first draft of the paper.

**Paper III** : Fabricated all samples (except for the polymer synthesis) and performed all the measurements (except the physical characteristics of the polymer and gravimetric experiments). Wrote the first draft of the paper.

**Paper IV** : Fabricated all samples (except for the polymer synthesis) and performed all the measurements (except the physical characteristics of the polymer). Wrote part of the first draft of the paper.

# Contents

|          |  |           |
|----------|--|-----------|
| <b>1</b> | <b>Introduction.....</b>                                   | <b>1</b>  |
| 1.1      | Sensors.....   | 2         |
| 1.1.1    | Nanoplasmonic Sensors.....                                 | 3         |
| 1.2      | Challenges in the Energy and Environmental Fields.....     | 5         |
| 1.2.1    | Hydrogen Economy.....                                      | 5         |
| 1.2.2    | Carbon Capture and Storage.....                            | 7         |
| 1.2.3    | Solar Energy Harvesting.....                               | 8         |
| 1.3      | This Thesis.....   | 10        |
| <b>2</b> | <b>Nanoplasmonics.....</b>                                 | <b>13</b> |
| 2.1      | Electrons in a Metal.....                                  | 13        |
| 2.2      | Localized Surface Plasmon Resonance.....                   | 14        |
| 2.2.1    | Understanding LSPR: The Electrostatic Approximation.....   | 16        |
| 2.2.2    | LSPR Dependence on Particle Size, Material, and Shape..... | 18        |
| 2.3      | LSPR Sensors.....  | 21        |
| 2.3.1    | Indirect Nanoplasmonic Sensing (INPS).....                 | 25        |
| <b>3</b> | <b>Hydrogen in Metals.....</b>                             | <b>27</b> |
| 3.1      | Metal Hydrides.....  | 27        |
| 3.2      | Hydrogen Sensors.....                                      | 30        |
| <b>4</b> | <b>Nanofabrication.....</b>                                | <b>33</b> |
| 4.1      | Spin Coating.....  | 33        |
| 4.2      | Plasma Etching.....  | 34        |
| 4.3      | Thin Film Deposition.....                                  | 35        |
| 4.3.1    | Physical Vapor Deposition.....                             | 35        |

|          |   |           |
|----------|---|-----------|
| 4.3.2    | Chemical Vapor Deposition.....  | 37        |
| 4.4      | Hole-Mask Colloidal Lithography .....   | 39        |
| 4.4.1    | Nanodisk Structures .....   | 41        |
| 4.4.2    | Layered Nanodisk Structures .....   | 42        |
| 4.4.3    | Indirect Nanoplasmonic Sensing Chips .....  | 43        |
| <b>5</b> | <b>Characterization Techniques.....</b>   | <b>45</b> |
| 5.1      | Electron Microscopy .....   | 45        |
| 5.1.1    | Scanning Electron Microscopy .....  | 46        |
| 5.1.2    | Transmission Electron Microscopy .....  | 47        |
| 5.2      | Optical Measurements .....  | 49        |
| 5.2.1    | Spectrophotometry .....   | 49        |
| 5.2.2    | Optical Measurements in Temperature-Controlled Vacuum Chamber ..  | 52        |
| 5.2.3    | Optical Measurements in Elevated Temperature under Gas Flow.....  | 53        |
| 5.2.4    | Data Analysis .....   | 53        |
| <b>6</b> | <b>Summary and Outlook .....</b>  | <b>55</b> |
| 6.1      | Summary of Appended Papers .....  | 55        |
| 6.2      | Outlook.....  | 56        |
| <b>7</b> | <b>Acknowledgements .....</b>   | <b>59</b> |
| <b>8</b> | <b>Bibliography .....</b>   | <b>61</b> |
| <b>9</b> | <b>Appendix.....</b>  | <b>71</b> |
| 9.1      | Matlab Program that Extracts Characteristic Plasmonic Readout Parameters<br>Using a Lorentzian Fit..... | 71        |



# 1 Introduction

Canary birds, small in stature with bright yellow feathers, were once a highly priced and fashionable commodity for Spanish and English kings<sup>1</sup> due to their ability to produce diverse and elaborate tweets. However, later on more people could get a hand on the bird and breed them themselves, and they became very popular throughout Europe. Unfortunately, fate did not mean well with canaries when they were used as an early warning system in coal mining in the 19<sup>th</sup> century. At that time when the industrial age soared, mining activities were expanded greatly which caused countless miners dying of gas poisoning. An ingenious (yet cruel) solution came up by using canaries as poisonous gas detectors. Birds are perfect gas detectors as they suck fresh air into their lungs both when they inhale and exhale; as opposed to us, humans, who only get fresh air when we inhale. Upon leakage of life-threatening gases such as carbon dioxide (CO<sub>2</sub>), carbon monoxide (CO) and methane (CH<sub>4</sub>), the canaries, normally very songful birds, would stop singing and eventually die, signalling the miners to exit the mine hurriedly. This cruel practice lasted very long until it was finally phased out in 1986<sup>2</sup> thanks to the development of handheld electronic gas detectors (and increasing awareness in animal welfare).



**Figure 1.1. Canary bird as toxic gas detector in coal mines.** An old picture showing a worker in a coalmine holding a caged canary bird. Canary birds were widely used in coal mines as poisonous gas detectors. When the singing of the birds weakened or eventually stopped (i.e. the birds were poisoned) the workers knew gas leakage had occurred and could run away for safety. The picture is taken from the web.<sup>3</sup>

At this point it is clear that the need to monitor aspects of our surroundings, due to concerns about the environment, our health and safety, has existed since the dawn of humanity. This has led to tremendous efforts and resources being devoted to the development of new *sensors* for a multitude of applications. This is closely linked to the fact that the last century has seen an impressive advancement of science and technology. New physics and materials were discovered and novel technologies were established. The culmination of this advancement is reflected in the number of tools and technologies that have replaced and/or improved once customary apparatus in our daily life, including sensors. Nevertheless, even though sensors have been developed for a variety of applications, most of them still suffer from problems such as low selectivity and/or sensitivity due to our ever increasing and more stringent demands. Clearly, the sensor performance boundaries should continuously be expanded and it has been proposed that developing nanoscale sensors may help to achieve this.

In the last few decades, nanoscience and nanotechnology has greatly revolutionized science and technology, as foreseen by Richard Feynman, a Noble Laureate and a *great* physicist, in his visionary lecture in 1959. In “*There is plenty of room at the bottom*” he noted that the revolution in science and technology would be driven by something *very* small.<sup>4</sup> The key to the nanoscale revolution is the new phenomena that arise when a system features nanometer dimensions. In this dimension range, the world is not the same as in the macroscopic world we are living in. Things that are observed at macroscopic scale may behave significantly, or even totally, different at the nanoscale. For example, the shiny look of our golden rings will become red, green, or blue, depending on the size, if it is shrunk to the nanoscale, as shown by Larsson *et al.* when they fabricated gold nanorings with various sizes of 75–150 nm (they do not even fit a bacteria’s “body”!).<sup>5</sup> Exploiting these new properties opens the door to new technological advances in almost every aspect of our lives.

One of the most interesting nanoscale phenomena is the so-called *localized surface plasmon resonance (LSPR)*. LSPR occurs in a metal particle smaller than the wavelength of light. It makes the nanoparticles exhibit efficient light scattering and absorption, depending on their size and shape. In short, these properties can be utilized as sensor transducer and, in fact, during the past decade a major field of LSPR sensors has emerged (detailed explanation will be given in **Chapter 2**). The fascinating properties of *tiny* metallic particles and their *huge* potential for improving the state-of-the-art of sensors, especially for applications in energy and environmental fields, are what have engaged me in the past couple of years. Therefore I am very eager to share this with the reader through this thesis.

## 1.1 Sensors

Sensors are already today omnipresent in our daily life, ranging from usage in casual activities, *e.g.* in consumer electronics (pressure, temperature, touch, etc., which contributed to \$22 billion market value in 2015!<sup>6</sup>), as well as in more critical contexts such as pollution monitoring. In general, a sensor is defined as a device that measures a physical quantity and

converts it into a signal that can be read by an observer or an instrument. The conversion is done by a transducer, which is an integral part of a sensor. Sensors can be classified according to several different criteria such as the form of energy picked up by the transducer, the quantity being measured, the technology used, or the application. The energy detected and converted by a transducer can furthermore be grouped into six different categories:<sup>7</sup>

1. Radiant/optical (*e.g.* photodetectors)
2. Mechanical (*e.g.* pressure sensors)
3. Gravitational (*e.g.* mass balances)
4. Electric (*e.g.* voltmeters)
5. Thermal (*e.g.* thermometers)
6. Magnetic (*e.g.* magnetic compass)

In general, optical sensors are attractive because they may offer wide dynamic range, multiplexing capabilities, electrical passiveness, high sensitivity, absence of electromagnetic interference and the possibility for remote sensing.<sup>7</sup>

In this thesis, optical LSPR sensors are the central focus. Expectedly, LSPR sensors will benefit not only from the generic features of optical sensors but also from effects (both positive as listed below but also, potentially, negative) that become available due to the nanoscale dimensions. These include faster response time, high localized sensitivity and small sample size. These features have been demonstrated widely using different types of sensors based on various nanoarchitectures and nanomaterials, including nanowires,<sup>8,9</sup> quantum dots,<sup>10,11</sup> carbon nanotubes<sup>12,13</sup> and graphene,<sup>14,15</sup> employing multiple transducing techniques.

### 1.1.1 Nanoplasmonic Sensors

As briefly mentioned before, the localized surface plasmon resonance (LSPR) phenomenon constitutes the heart of the research field known as *nanoplasmonics* and is one of the most interesting phenomena occurring at the nanoscale. LSPR occurs in a metal particle smaller than or close to the wavelength of light. Despite technological applications of LSPR being relatively young, LSPR has empirically been exploited for nearly 1700 years, as shown by the *Lycurgus cup* crafted by a Roman glass artist from the 4<sup>th</sup> century A.D., see **Figure 1.2**. The Roman craftsman successfully incorporated small colloidal metallic particles of gold, silver and copper into the glass,<sup>16</sup> which results in the different colors exhibited when the glass is seen in reflected and transmitted light. The reason why the cup displays different color is the different scattering and absorption, respectively, exhibited by the metal nanoparticles.

Although the utilization of noble metal nanoparticles has started long time ago (it is speculated that the Romans did not know that nanoparticles were involved in the coloration phenomenon discussed above<sup>18</sup>) it is not until the last century when the characteristic optical properties of noble metal nanoparticles were unearthed in the context of colloidal chemistry,

which allowed their controlled synthesis. The first step towards understanding the phenomenon was taken by Gustav Mie, a German scientist, who explained the strong interaction of light with metal nanoparticles by analytically solving Maxwell's equations.<sup>19</sup> Since then, the fundamental understanding of LSPR in nanoparticles has become significantly deeper and with the development of nanofabrication that allows production of nanoparticles with controlled shape and size, a plethora of applications has been demonstrated, especially in the last two decades. Among these applications are that LSPR can be utilized in optical waveguides,<sup>20-22</sup> to improve the resolution of microscopes,<sup>23</sup> as therapy agent in tumour treatment<sup>24-26</sup> and as highly sensitive chemical and biological sensors (the physics behind this will be discussed later in **Chapter 2**).<sup>27-29</sup>



**Figure 1.1. The Lycurgus cup.** The famous Roman-era cup shows different coloration, i.e. green and red, when it is viewed in reflected and transmitted light, respectively. The phenomenon is due to the different absorption and scattering efficiencies of the metal nanoparticles dispersed in the glass. The photos are reproduced from the web page of the British Museum.<sup>17</sup> © Trustees of the British Museum.

As previously mentioned, many of today's sensors suffer from low sensitivity, long response time, short lifetime, large size, etc., in particular in emerging application areas. LSPR-based sensors have shown potential to tackle these problems. In the past decade, a large number of different variations of LSPR sensors have been developed. They have in common that they are characterized by high local (few tens of nanometers from the sensor particle surface) sensitivity, single particle sensing possibility, high temporal resolution, real time and remote detection, label-free detection of analytes, and *in situ* operating capability.<sup>30,31</sup> In addition, all of these properties come with the potential for vast miniaturization and parallelization, promising an interesting platform for practical sensing applications. This potential is so far closest to commercial realization in the rapidly expanding fields of plasmonic biosensing,<sup>27,30,32</sup> gas detection<sup>33-35</sup> and nanomaterials science.<sup>36</sup>

## 1.2 Challenges in the Energy and Environmental Fields

Two of the grandest challenges in the 21<sup>st</sup> century are our supply with sustainable energy and climate change.<sup>37</sup> These two are also closely related to each other. Today, we are still hugely relying on fossil fuels (*e.g.* coal, oil) that are not sustainable and produce CO<sub>2</sub> as by-product upon energy production, the gas most responsible for the global warming effect.<sup>38</sup> Thus, numerous laws, regulations, science and technological advancements are pointed towards solving these problems. “Sustainable energy” is the buzzword nowadays. Indeed, sustainable energy sources are one of the main solutions for the aforementioned problems and they may even help solving another problem, that is, the “poor-rich gap”, as they provide “unlimited” and (as the ultimate the goal) cheap energy supply without CO<sub>2</sub> as by-product upon consumption. The work presented in this thesis is aligned with this goal. Thus we direct the nanoplasmonic sensing technologies developed in this thesis to be a small part of all the new technical solutions needed to solve the sustainable energy challenge.

### 1.2.1 Hydrogen Economy

Imagine a situation where the fuel we use (*e.g.* for transportation or in industry) generates *only* water as by-product and will never run out. Well, actually, this is not at all pure imagination. Hydrogen, the smallest yet most abundant element in the universe, if used as fuel, actually carries most energy per unit mass; about three times the mass energy density of gasoline and seven times of the one of coal.<sup>39</sup> Thus, in the 1970ties, the vision of a world powered by hydrogen was coined; the hydrogen economy.<sup>40</sup> In this scenario hydrogen is the center of a fully sustainable and carbon-free energy cycle. The idea is to use other sustainable energy sources (*e.g.* solar energy) to split water into hydrogen and oxygen. The hydrogen produced is then stored until the energy is needed. Finally, when the hydrogen is combusted or used to produce electricity in a fuel cell, the only waste product is water. This creates a truly sustainable energy cycle that is free from CO<sub>2</sub> emissions (**Figure 1.3**).

Despite its very appealing prospects described above, we have not seen the hydrogen economy implemented at a large scale yet (though last year, 2014, Toyota and Hyundai released their first commercial hydrogen fuel cell cars). The reason is that there still are numerous technological challenges that need to be addressed before the concept can reach widespread use, for example to find efficient ways to produce, store and utilize hydrogen.

Also, safety aspects of the hydrogen economy have to be addressed. Hydrogen is a highly flammable gas at ambient temperatures when mixed with air (flammability range: 4–75 vol. %). Furthermore, the energy input needed to ignite oxygen-hydrogen mixtures is very low; even an invisible static spark can be enough. As a consequence, the development of reliable hydrogen sensors is crucial in the deployment of a *safe* hydrogen economy. As an example, more than 15 hydrogen sensors are installed in the commercial hydrogen fuel cell cars available since last year to ensure a safe operation. With mass production and widespread use of hydrogen as a fuel around the corner, stringent requirements have been set for the development of next-generation hydrogen sensors,<sup>43</sup> as shown in **Table 1.1**. Even outside

automotives, hydrogen sensors are already today widely used in industrial processes.<sup>44</sup> To reach the set targets, technological breakthroughs have to be made, and I am convinced that plasmonic sensing holds (one of) the key(s).

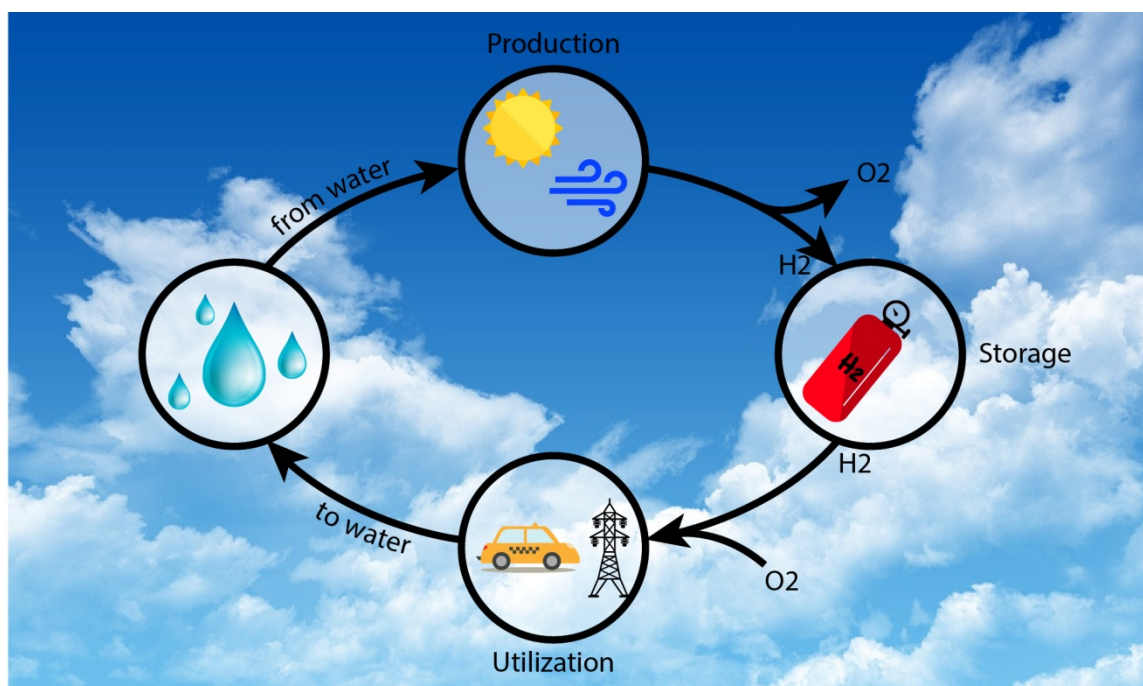


**Figure 1.3. The hydrogen economy.** Hydrogen is produced by splitting water with electricity generated from sustainable energy sources such as solar and wind energies. The hydrogen is stored and distributed to user where it is converted back into energy in a fuel cell. The only waste product is water and thus the loop is closed. All the icons used in the schematic and the background picture are taken from <sup>41</sup> and <sup>42</sup>, respectively.

**Table 1.1 Requirements for hydrogen sensors for stationary and automotive applications.**<sup>43</sup>

|                                  | Stationary                                  | Automotive     |
|----------------------------------|---|----------------|
| Measuring range                  | Up to 4 vol.% H <sub>2</sub> (survive 100%) |                |
| Lower detection limit            | < 0.1 vol. %                                |                |
| Response time (t <sub>90</sub> ) | < 30 s                                      | < 1 s          |
| Response time (t <sub>10</sub> ) | < 30 s                                      | < 1 s          |
| Accuracy                         | ±10 %                                       | ±5 %           |
| Ambient temperature              | -20 to +50 °C                               | -40 to +125 °C |
| Ambient pressure                 | 80–110 kPa                                  | 62–107 kPa     |
| Ambient relative humidity        | 20–80%                                      | 0–100%         |

## 1.2.2 Carbon Capture and Storage

CO<sub>2</sub> emissions from fossil fuelled vehicles and industrial processes constitute 65 % of global greenhouse gases causing increasing global temperature.<sup>38,45</sup> At the individual level, CO<sub>2</sub> pollution may cause an excessive amount of CO<sub>2</sub> in the blood, which typically results in a serious and sometimes fatal condition characterized by headache, nausea and visual disturbances.<sup>46,47</sup> Therefore, numerous mitigation strategies for CO<sub>2</sub> emission reduction are suggested or actively being applied. One particular direction is the *Carbon Capture and Storage (CCS)* scheme whose goal is to capture waste CO<sub>2</sub> from large point sources (e.g. fossil fuel power plants), transport it to a storage site and deposit it where it will not enter the atmosphere (or reuse it in a considerable amount for other industrial processes).

The deployment of CCS schemes requires close collaboration between different fields, ranging from politics to technology. One of the consequences of the increasing interest in CCS in the technological field is the accelerated search for materials that can capture CO<sub>2</sub>. Numerous kinds of materials have been reported and used: e.g. (liquid) amines, metal oxides, zeolites, metal-organic frameworks (MOFs) and polymers.<sup>48–52</sup> The last three of the mentioned examples belong to the class of mesoporous materials, which are attractive for CCS due to their very high specific surface area (the current record for the highest specific surface area for porous material is hold by NU-109 and NU-110, both belong to a class of MOF, whose surface area reaches 7000 m<sup>2</sup>/g; that is, one kilogram of the material contains an internal surface area that could cover seven square kilometers!<sup>53</sup>).

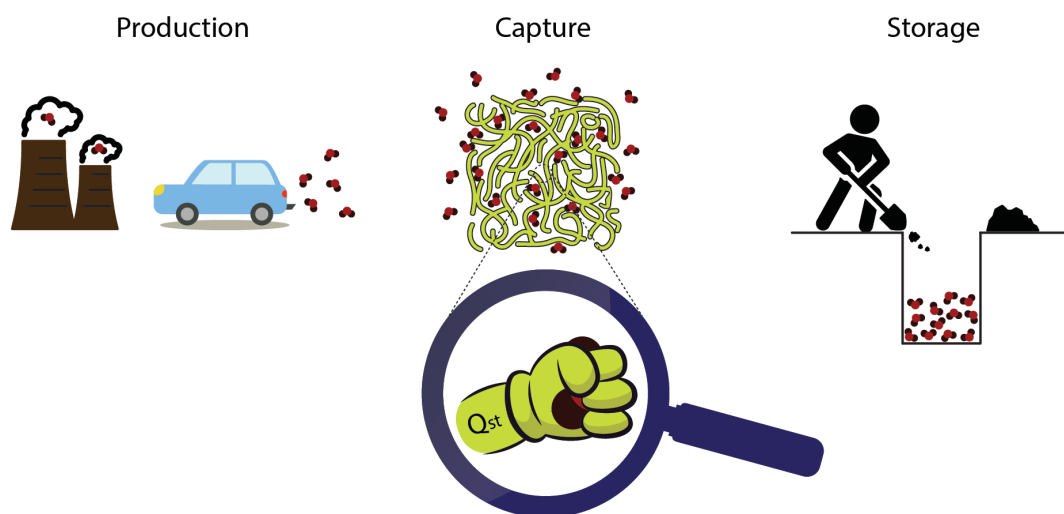


**Figure 1.4. Carbon Capture and Storage.** Carbon Capture and Storage (CCS) is the process of capturing waste CO<sub>2</sub> from large point sources (e.g. fossil fuel power plant), transporting it to a storage site, and depositing it where it will not enter the atmosphere, normally an underground geological formation. One of the ways to capture the CO<sub>2</sub> is by utilizing sorbent materials that are able to selectively adsorb the CO<sub>2</sub> from gas mixtures. The interaction strength of CO<sub>2</sub> with the sorbent materials is expressed through the isosteric heat of adsorption ( $Q_{st}$ ). Some of the icons used in the schematic are taken from <sup>41</sup>.

Capture of CO<sub>2</sub> with these materials is based on the idea that CO<sub>2</sub> *selectively* adsorbs from gas mixtures and can be recovered as nearly pure CO<sub>2</sub> by cyclically increasing the temperature or decreasing the pressure.<sup>48</sup> For a successful CO<sub>2</sub> capture (and release), the CO<sub>2</sub>-adsorbent interaction strength should be engineered in an optimal way.<sup>54</sup> It should be strong enough so that CO<sub>2</sub> cannot easily escape at conditions characteristic for the environment from which it is to be removed (in other words, these conditions can vary greatly for specific applications) but also not too strong so that complete release can be achieved by mild heating to make the process energy efficient.

The interaction strength of CO<sub>2</sub> with a sorbent is typically assessed by measuring the *isosteric heat of adsorption* ( $Q_{st}$ ) using various methods based on gravimetric and volumetric measurement principles. Gravimetric techniques are complicated by buoyancy and Knudsen diffusion at low pressure, while volumetric techniques need accurate dead space determination for volume correction. Furthermore, both methods have a common requirement for accurate initial determination of sample weight and/or volume.<sup>55</sup> Additionally, porous polymer systems (as well as, *e.g.*, MOFs) potentially show swelling upon CO<sub>2</sub> adsorption, which further complicates their analysis.<sup>56</sup> Therefore it is very appealing to develop new experimental strategies for the scrutiny of CO<sub>2</sub> sorption processes in such materials. Ideally, the experimental methodology developed is easy to use, yet accurate, and allows rapid characterization for efficient screening of new materials for CCS. Using indirect nanoplasmonic sensing, I demonstrate in **Paper III** that optical spectroscopy based on plasmonics has the potential to be such a technique.

### 1.2.3 Solar Energy Harvesting

Sunlight is the most powerful and abundant sustainable energy source available on Earth. The energy arriving from sun to the Earth's surface in two hours is enough to supply our global energy demand for a year. This translates to that covering only 0.16 % of the Earth's surface with 10 % efficient solar to electricity conversion systems would provide 20 TW of power,<sup>57</sup> which would exceed the projected global yearly energy supply needed in 2030.

Solar energy can be harvested in two basic approaches being developed today: solar-thermal technology and photovoltaics (PV). In the second approach, a PV cell (solar cell) produces electricity directly from sunlight via physical processes in specially designed materials. Today's solar cells available on the market are dominated by (single crystalline) silicon technology (*ca.* 82% in 2012<sup>58</sup>) with current record efficiency of 22 % solar to electricity conversion.<sup>59</sup> The established silicon-based solar cells are what is known as the "first generation". Following this, with the aim to lower PV device cost, second and third generation solar cells were developed. The second generation is also called thin-film PVs. It still relies on inorganic semiconductor materials, however, with higher absorption coefficients compared to single crystalline silicon. This makes it possible to use thin films to achieve efficient light absorption, which, in turn, facilitates the use of polycrystalline or amorphous (less-perfect) materials without drastic loss in efficiency. This, finally, lowers the cost for the

devices. The third generation introduces entirely new materials, some of which are organic components. These PVs are cheap but their efficiency and *stability* have to be improved before they can enter the PV market at a large scale. Examples of third generation solar cells are dye-sensitized solar cells and polymer solar cells.

In the past decade, third generation polymer solar cells have attracted considerable attention due to their potential advantages such as cost-effective processing from solution, which can be accomplished by rapid roll-to-roll coating techniques on flexible substrates. Furthermore, power conversion efficiencies above 10 % have recently been reported.<sup>60</sup> Current state-of-the-art of the light absorber layer in a PV relies on the intermixed blend of a donor polymer and an acceptor polymer. To date, P3HT and a fullerene derivative PC<sub>61</sub>BM are the most studied donor and acceptor materials in organic PVs, respectively.<sup>61</sup> However, polymers exhibit a characteristic phase transformation at certain temperatures that greatly affects their properties. The so-called *glass transition temperature* ( $T_g$ ) is, in the simplest explanation, the critical temperature at which an amorphous material changes from being *glassy* to being *rubbery*. Glassy in this context represents hard and brittle (thus relatively easily to break, polymer chains are “frozen”), while rubbery means elastic and flexible (polymer chains become mobile and free to exert chain motion). The difference in the mobility of the polymer chains dictates, in the scope of solar cell applications, the polymer’s thermal stability, mechanical properties and de-wetting and delamination characteristics.<sup>62</sup> For example, it has been reported that polymer processing (*e.g.* annealing) above  $T_g$  leads to drastic decrease in solar cell efficiency.<sup>63–66</sup>

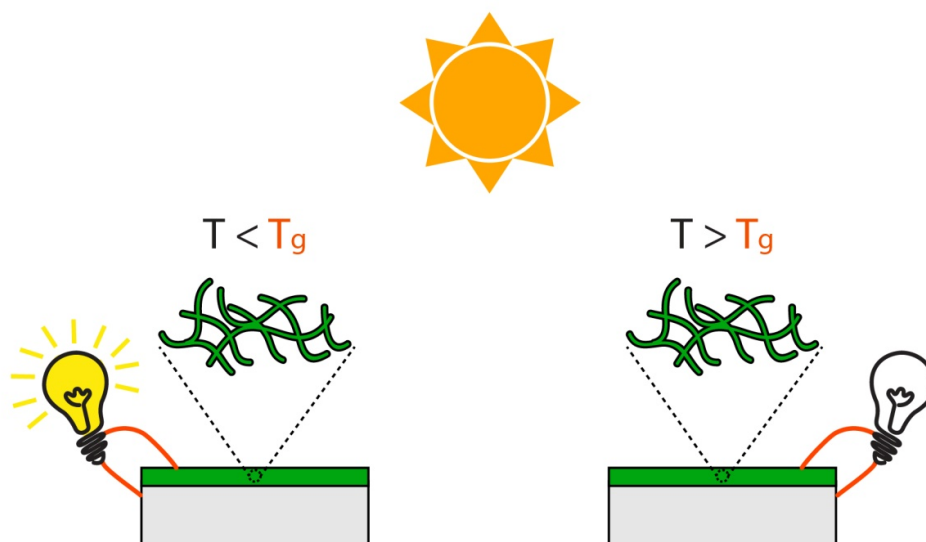


**Figure 1.5. Glass transition temperature effects on the performance of polymer solar cells.** The glass transition temperature ( $T_g$ ) in polymer systems constitutes a transition point where significant change in properties of the latter occurs. Among other, it has been reported that heating of an organic PV device above its  $T_g$  leads to a decrease in the solar cell efficiency. Thus, knowledge of  $T_g$  of thin film organic PV absorber layers is essential in order to optimize the processing temperature during solar cell preparation, as well as their operating temperature.

Therefore, an intimate understanding of  $T_g$  in the thin polymer blend films used as light absorbers in organic PVs, as well as strategies to increase this critical parameter, are required in order to fully capitalize on the potential of organic PVs.

Experimentally, the  $T_g$  of (bulk) polymers can be measured with a number of techniques. Differential scanning calorimetry (DSC) and ellipsometry are widely used methods. However, since the absorber layer of polymer solar cells is typically on the order of 100 nm thin, deviations from the *bulk* thermal properties must be anticipated,<sup>67–69</sup> and the use of standard techniques such as differential scanning calorimetry (DSC) is no longer possible because it is not sensitive enough for such thin films. Hence, accurate determination of the thin-film thermal behavior of polymer semiconductor systems is today limited to variable-temperature ellipsometry<sup>62,70</sup> where it has revealed that the  $T_g$  of conjugated photovoltaic polymer thin films with a thickness of less than 100 nm can display a significant deviation from the bulk.<sup>71–75</sup> However, correct determination of  $T_g$  from ellipsometry requires precise optical properties of the used substrate. Therefore, more direct, sensitive and robust analytical tools have to be developed for the investigation of the thermal behaviour of thin film polymer semiconductor systems. Nanoplasmonic sensing is attractive for this purpose as it has previously been used to determine the thickness dependence of  $T_g$  of non-conjugated polymers such as PMMA and polystyrene.<sup>76</sup>

### 1.3 This Thesis

This thesis comprises work related to *developing* and *establishing* nanoplasmonic sensors to tackle some of the challenges in the fields described above, *i.e.* hydrogen sensors, CCS and organic PVs.

In the first part of my work, I propose a bottom-up nanofabrication method to create metallic alloy nanoparticle arrays on surfaces for plasmonic applications in general, and hydrogen sensing in particular (**Paper I**). This method is then utilized in **Paper II** to fabricate AuPd alloy nanoparticle arrays to be used as optical plasmonic hydrogen sensors, in an attempt to actively contribute to the development of a hydrogen economy. The performance of these sensors is assessed and compared to the requirements set for automotive industries previously summarized in **Table 1.1**.

The second part of my work establishes indirect nanoplasmonic sensing (INPS) as an analytic experimental tool to assess the key properties of two types of materials for energy applications. **Paper III** constitutes an attempt to utilize INPS as accurate method for determining CO<sub>2</sub> adsorption energetics on mesoporous adsorbents. Specifically, we study PIM-1,<sup>77,78</sup> a material that belongs to the rising class of microporous polymers and exhibits high CO<sub>2</sub> permeability and selectivity,<sup>79–81</sup> and benchmark the results with the ones obtained from traditional analysis using a gravimetric method.

Finally, **Paper IV** scrutinizes the glass transition temperature of a donor polymer, of a fullerene acceptor, and of their ternary blend (used in light absorber layers in some of today's

most efficient organic PVs<sup>82,83</sup>) as a function of film thickness. Specifically, the TQ1 donor polymer (conversion efficiency of up to 7%<sup>84,85</sup>), and PC<sub>61</sub>BM:PC<sub>71</sub>BM fullerene mixtures are investigated. The film thickness dependence of  $T_g$  of this system has before not been reported due to its specific properties, *i.e.* only minuscule change in its refractive index and volume during glass transition, which makes it undetectable for conventional techniques.

The organization of the remainder of this thesis is as follows: **Chapter 2** introduces the background physics to the LSPR phenomenon, with particular focus on the mechanisms through which metallic nanoparticles supporting LSPR can be utilized as sensors. **Chapter 3** provides an overview of metal hydride systems, including their exploitation as hydrogen storage materials and, as of particular interest here, signal transducers in hydrogen sensors. **Chapter 4** describes the nanofabrication techniques that I have developed and employed to make my samples, and **Chapter 5** explains the different characterization methods I have used to assess the fabricated structures and sensors. Finally, **Chapter 6** summarizes the main results obtained in the appended papers, and I present a short outlook.



# 2 Nanoplasmonics

The field of nanoplasmonics, which explores localized surface plasmon resonance phenomena in noble metal nanoparticles, has been around for about two decades. In simplest terms, a plasmon resonance is a *coherent collective oscillation* of the free electrons in a metal. In the particle analogy it can be understood as the quantum of the plasma oscillation (thus the *-on* suffix in plasmon). I believe this summary may not be sufficient for most of the readers and so this chapter is written to briefly introduce the field of plasmonics and the concept of the localized surface plasmonic resonance. Furthermore, a well-developed application of localized plasmons, their use in sensors, which is a central topic of this thesis, will also be addressed with main focus on the concept of indirect nanoplasmonic sensing.

## 2.1 Electrons in a Metal

In order to understand the optical properties of materials one should, at the beginning, refer to an approach developed by H. A. Lorentz<sup>86,87</sup> to explain how electrons in a metal behave under the influence of an external electric field. In his model, better known as the *Lorentz Model*, Lorentz described the optical properties of a material in terms of the response of a classic harmonic oscillator to an external driving force. Electrons of matter are considered to be a collection of identical, independent, isotropic harmonic oscillators oscillating back and forth around their equilibrium position, *i.e.* the positively charged cores of the atom in the lattice of the solid. When an external electric field  $\mathbf{E}(\mathbf{x}, t)$  acts upon these oscillators they follow the equation of motion

$$m_e \ddot{\mathbf{x}} + m_e \Gamma \dot{\mathbf{x}} + k \mathbf{x} = -e \mathbf{E}(\mathbf{x}, t) \quad (2.1)$$

where  $m_e$  is the mass of the electron,  $\mathbf{x}$  is the displacement from equilibrium,  $\Gamma$  is the damping constant,  $k$  is the spring constant of the harmonic oscillator and  $e$  is the electronic charge. If the applied field is harmonic with frequency  $\omega$  and the oscillation amplitude is small so that the field is approximately spatially constant, equation 2.1 has a single solution describing the induced dipole of a single oscillating electron as

$$\mathbf{p} = -e \mathbf{x} = \frac{e^2}{\omega_0^2 - \omega^2 - i \Gamma \omega} \mathbf{E} \quad (2.2)$$

where  $\omega_0$  is the resonance frequency of the oscillator defined as

$$\omega_0 = \sqrt{\frac{k}{m_e}} \quad (2.3)$$

Assuming a system consisting of a large number,  $N$ , of independent electrons, the polarization  $\mathbf{P}$  (dipole moment per unit volume) can be calculated by multiplying  $N$  with equation 2.2. By using the constitutive relation<sup>86</sup>

$$\mathbf{P} = \varepsilon_0(\varepsilon - 1)\mathbf{E} \quad (2.4)$$

A complex dielectric function  $\varepsilon(\omega)$  for a system with a large numbers of independent electrons can then be defined as

$$\varepsilon(\omega) = 1 + \frac{\omega_P^2}{\omega_0^2 - \omega^2 - i\Gamma\omega} = \left(1 + \frac{\omega_P^2(\omega_0^2 - \omega^2)}{(\omega_0^2 - \omega^2)^2 + \Gamma^2\omega^2}\right) + i \frac{\omega_P^2\Gamma\omega}{(\omega_0^2 - \omega^2)^2 + \Gamma^2\omega^2} \quad (2.5)$$

The resonance frequency,  $\omega_0$ , originates from the restoring force experienced by an electron bound to an atom while the damping constant,  $\Gamma$ , quantifies the inelastic processes associated with it, and lastly the plasma frequency,  $\omega_P$ , reads as

$$\omega_P = \sqrt{\frac{Ne^2}{m_e\varepsilon_0}} \quad (2.6)$$

For an electric field with frequency  $\omega < \omega_p$  the electrons will follow it and the dielectric function  $\varepsilon$  is complex (*i.e.* has a real and imaginary part, see equation 2.5). Within the metal the field decays exponentially with the distance from the metal-dielectric interface. Therefore, the incident field is attenuated and the electromagnetic field is reflected back from the surface. If the opposite situation of  $\omega > \omega_p$  occurs, the electrons inside the metal cannot respond fast enough to screen the electric field. The refractive index  $\varepsilon$  is then real and the metal behaves as a dielectric material *i.e.* the optical field is partly refracted and partly reflected. The bulk plasma frequencies of metals are located in the ultraviolet spectral range, which explains why they appear shiny and reflective for the human eye.

## 2.2 Localized Surface Plasmon Resonance

When a metal entity becomes smaller or comparable to the wavelength of near-visible light its optical properties change dramatically. Under this circumstance the free electrons of the particle can oscillate collectively when excited by the external optical electromagnetic field with appropriate frequency. The oscillation typically decays within few femtoseconds due to the significant damping (imaginary part of  $\varepsilon$ ) characteristic for metals. The displaced electrons (together with the rigid positively charged atomic cores) create a polarization field of their own, which drives them back towards the equilibrium position. Due to the inertia, overshoot occurs even in the absence of the external field. When the frequency of the applied field matches with the system's eigenfrequency a collective coherent resonance occurs. The size of the nanoparticle also imposes a boundary condition that prohibits the formation of a propagating longitudinal charge density wave, *i.e.* like in the case of bulk and surface plasmon resonance. Instead, in a simple picture, a standing electron wave oscillation with respect to the atomic core is accomplished. Hence the name *localized surface plasmon resonance (LSPR)*.

LSPR is one of the best examples of how things may change significantly at the nanoscale. At the LSPR frequency, metal particles effectively scatter and absorb light, which gives rise to a strong peak in their light extinction (*i.e.* sum of scattering and absorption) spectrum. Furthermore, the charge separation at the particle surface gives rise to a strong electric field close to the surface. **Figure 2.1** shows a schematic illustration of the coherent motion of the free electrons under the applied field. It corresponds to an oscillating time-dependent electric dipole, which gives rise to an induced electric field due to the charge separation. Two higher order modes of the LSPR, which may play a role for bigger particles, are also shown.

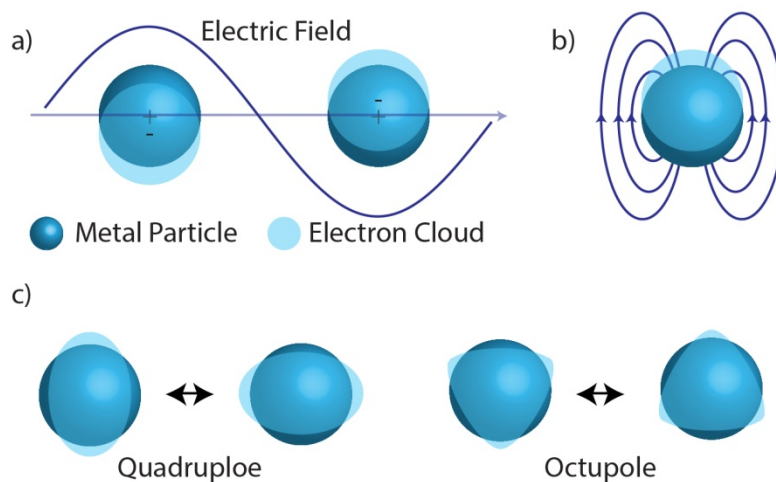


**Figure 2.1. Schematic illustration of localized surface plasmon resonance in a small metal sphere.** (a) The external electromagnetic field created by irradiated light pushes the electrons of a nanoparticle out of their equilibrium positions relative to the positively charged atomic cores. The free electrons oscillate collectively with largest amplitude when the light frequency matches their resonance or eigenfrequency. (b) Due to the oscillating charges, which lead to a polarization of charge on the surface of the nanoparticle, a strong electric field is developed in the vicinity of the particle. (c) For larger nanoparticles (relative to the wavelength), higher modes of the LSPR exist, for example quadrupole and octupole modes.

LSPRs can typically be excited in the ultraviolet (UV), visible, and near infra-red (NIR) range of the electromagnetic spectrum. The excitation represents a time-dependent dipole that generates a strong local field, which is superimposed on the external field that drives the oscillation. Thus, due to the resonant nature of the excitation, the local field around the nanoparticles (near-field) is *enhanced*. This field can act as a *probe* of the nanoparticles' surrounding and makes the LSPR very sensitive to changes of the permittivity of the medium in the vicinity of the particle, as *e.g.* induced by molecular adsorption on the particle surface. Higher refractive index of the surrounding means higher polarizability, which in turn increases the screening of the dipolar field of the LSPR. The increased screening dampens the electron oscillation and, thus, decreases its energy (spectrally red-shifts the resonance, *i.e.* moves it towards longer wavelength). The plasmon energy is one key parameter in the characterization of LSPR, and it is also commonly used as the main readout in sensing

applications.<sup>27,30</sup> A detailed explanation of the sensing applications based on LSPR will be given in **Section 2.3**.

The lifetime of a typical LSPR excitation is about 5-25 femtoseconds, depending on particle size, shape and material. After excitation the plasmon dissipates either via electron-hole pair excitation and, ultimately, production of heat, or via radiative decay where a photon of the same energy as the incident one is re-emitted from the particle.<sup>88,89</sup> Light that enters the first decay channel is referred to as being *absorbed* by the nanoparticle.

The second channel corresponds to an elastic scattering process of electromagnetic energy by the induced dipole and is referred to as *scattering*. This occurs since LSPR can be described as time-dependent dipole, which radiates electromagnetic energy, just as the radiowave analogue of a Hertz antenna.

The sum of absorption and scattering is called optical *extinction*, which corresponds to the total attenuation of the electromagnetic wave, according to the optical theorem, as it traverses a particle. The efficiency of the two decay mechanisms can be expressed through their respective cross-sections (*i.e.* how efficient the processes are). The analytical expressions for absorption, scattering, and extinction cross section of a nanoplasmonic particle much smaller than the wavelength are shown below

$$\sigma_{abs} = k\text{Im}(\alpha) \quad (2.7)$$

$$\sigma_{sca} = \frac{k^4}{6\pi} |\alpha|^2 \quad (2.8)$$

$$\sigma_{ext} = \sigma_{abs} + \sigma_{sca} \quad (2.9)$$

where  $\alpha$  is the material polarizability (see below) and  $k$  is the wave vector.

The extinction cross section offers a convenient way to describe the interaction between light and nanoparticles. For a non-transparent object that does not resonantly interact with the electromagnetic field, the extinction cross section is equal to the projected geometric area of the particle and independent of the wavelength, *i.e.* only the light directly impinging on the particle will not be transmitted. For the case of strongly interacting particles the extinction cross section depends on the wavelength and can be significantly larger than the projected geometric area of the particle. This is the reason why plasmonic nanoparticles look colored (see *e.g.* Lycurgus Cup in **Chapter 1**). When white light hits the particles, a fraction of the wavelengths of the incident light is attenuated, leaving the rest of the wavelengths transmitted, hence creating the “colored” appearance of the cup.

### 2.2.1 Understanding LSPR: The Electrostatic Approximation

A simple way to understand LSPR is the electrostatic approximation in the so-called quasi-static regime. This model considers the particle diameter  $D$  to be small compared to the

wavelength of light ( $D \ll \lambda$ ), which means that, in a first approximation, the electron oscillation of the plasmon can be modeled as a point electric dipole. The mathematical form can be constructed if one considers a homogeneous, isotropic nanosphere placed in an arbitrary medium and subjected to a time-dependent external field  $\mathbf{E}_0 e^{-i\omega t}$ . The induced local field of the particle then superimposes with the applied field, creating a dipole moment that can be described as

$$\mathbf{P}(\omega) = \varepsilon_d \alpha(\omega) \mathbf{E}_0 e^{-i\omega t} \quad (2.10)$$

where  $\varepsilon_d$  is the dielectric constant of the surrounding medium and  $\alpha(\omega)$  is the dipole polarizability of the nanosphere. Gustav Mie, a German physicist, presented the exact solution of the light-metal nanoparticle interaction by solving Maxwell's equation more than a century ago.<sup>19</sup> According to his work, famously known as Mie theory, the polarizability  $\alpha(\omega)$  of the nanosphere reads as

$$\alpha(\omega) = 4\pi \left(\frac{D}{2}\right)^3 \frac{\varepsilon(\omega)_m - \varepsilon_d}{\varepsilon(\omega)_m + 2\varepsilon_d} \quad (2.11)$$

where  $\varepsilon_m(\omega)$  is the complex dielectric function of the nanosphere material. The magnetic permeabilities are assumed to be as in vacuum for both sphere and the external medium; a reasonable assumption for optical frequencies.<sup>87</sup> From equation 2.11 one can learn that the polarization becomes very large when the denominator is equal to zero (at resonance), *i.e.*  $\varepsilon_m(\omega) = -2\varepsilon_d$ . This condition requires the dielectric constant of the particles to have a negative real part  $\varepsilon_1(\omega)$  and, preferably, a small imaginary part  $\varepsilon_2(\omega)$  (*i.e.* small losses) for a strong polarization to occur. Inserting the Drude dielectric function into the expression for the dipole polarizability (equation 2.11) yields

$$\alpha(\omega) \approx 4\pi \left(\frac{D}{2}\right)^3 \frac{\omega^2_{LSPR}}{\omega^2_{LSPR} - \omega^2 - i\Gamma\omega} \quad (2.12)$$

where

$$\omega_{LSPR} = \frac{\omega_p}{\sqrt{1 + 2\varepsilon_d}} \quad (2.13)$$

or, if we use wavelength instead of frequency as we commonly do in measurements:

$$\lambda_{LSPR} = \lambda_p \sqrt{1 + 2\varepsilon_d} \quad (2.14)$$

where  $\lambda_{LSPR}$  is the localized surface plasmon wavelength. The  $\lambda_{LSPR}$  is generally smaller than the bulk plasmon's  $\lambda_p$ . From equation 2.14 it is clear that the spectral position of the LSPR in the quasi-static limit depends purely on the surrounding dielectrics (*i.e.*  $\varepsilon_d$ ) and the material itself (reflected through  $\lambda_p$ ). However this is not entirely true since for very small particles ( $< 10$  nm) the dielectric function of the metal is size-dependent. For larger particles, size-dependent retardation effects also influence the LSPR spectral position.<sup>87</sup> These effects will be explained further in the next section.

One can also insert the dipole polarizability (equation 2.11) into the expressions of scattering and absorption cross sections (equation 2.7 and 2.8). This yields

$$\sigma_{abs} = k\text{Im}(\alpha) = 4\pi k \left(\frac{D}{2}\right)^3 \text{Im} \left( \frac{\varepsilon(\omega)_m - \varepsilon_d}{\varepsilon(\omega)_m + 2\varepsilon_d} \right) \quad (2.15)$$

$$\sigma_{sca} = \frac{k^4}{6\pi} |\alpha|^2 = 8\pi \left(\frac{D}{2}\right)^6 k^4 \left( \frac{\varepsilon(\omega)_m - \varepsilon_d}{\varepsilon(\omega)_m + 2\varepsilon_d} \right)^2 \quad (2.16)$$

One can readily observe that absorption is proportional to the sphere volume ( $D^3$ ) while scattering is proportional to the square of the volume ( $D^6$ ). Thus, for very small particles, the absorption cross section dominates, while the scattering cross section dominates in larger particles. For example in gold nanospheres and nanodisks, this transition occurs for particle diameters around 80 nm and 100 nm,<sup>90,91</sup> respectively. An example of an extinction spectrum (that is, the sum of absorption and scattering) for an array of plasmonic nanodisks fabricated by hole-mask colloidal lithography (explained in **Chapter 4**) is plotted in **Figure 2.2**.

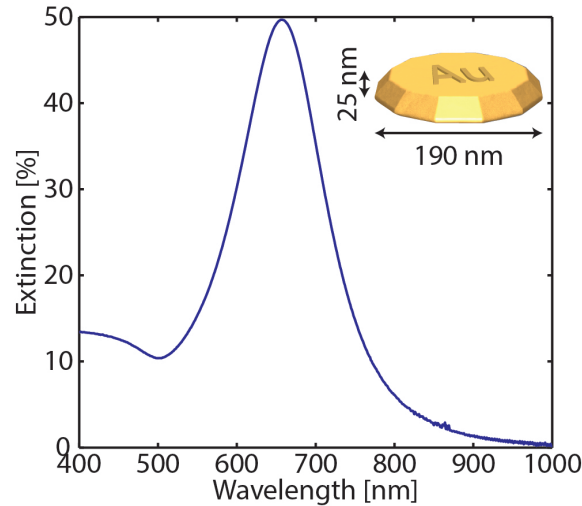


**Figure 2.2.** Extinction spectrum of an amorphous array of gold nanodisks with diameter of 190 nm and height of 25 nm, fabricated by hole-mask colloidal lithography (HCL) on glass. LSPR gives rise to a strong extinction peak due to efficient scattering and absorption by the gold nanoparticles.

### 2.2.2 LSPR Dependence on Particle Size, Material, and Shape

The previous discussion of the LSPR phenomenon was entirely based on the spherical particle approximation in the quasi-static regime, which is sufficient to give a basic idea about LSPR. However, in reality, various shapes and sizes of nanoparticles can be fabricated and are used for real applications. Therefore, since the polarizability of differently shaped particles is not the same as for a sphere, the scattering and absorption characteristics of such particles are different. It is thus essential to have extended models and approaches to explain the plasmonic

properties of more complex nanostructures. By knowing all the factors defining the LSPR one can then freely “design” the resonance to be most suitable for a specific application. Below a short discussion of the role of size/shape and material composition of the nanoparticle on the LSPR is presented.

For a particle larger than the quasi-static approximation range (*i.e.* where  $D \ll \lambda$  no longer applies) retardation effects and radiation damping become very important. Retardation of the applied field arises when the particle size is comparable to the wavelength and the field distribution is no longer homogeneous over the entire particle. A second retardation effect affects the field inside the particle since it takes time for the dipolar field to spread over the particle due to the finite speed of light. This retards the formation of the dipole and leads to a phase shift between the dipolar plasmonic and the exciting field of the irradiated light wave. These retardation effects induce a spectral red shift of the plasmon resonance, as well as peak broadening.<sup>92</sup>

Radiation damping originates from the energy loss of the time-dependent dipole via emission of radiation. This radiative plasmon decay channel thus becomes rapidly more significant for bigger particles since the dipole is proportional to the size of the nanoparticles, and the scattering cross section scales with  $D^6$  (see equation 2.8). Radiation damping also introduces a spectral red-shift, an increase in plasmon line width and a decrease in the resonance intensity.<sup>93</sup> Larger nanoparticles also feature multipolar modes (see **Figure 2.1c** for the case of nanosphere particles), which means that the resonance band splits into several peaks which appear at shorter wavelength than the dipolar peak in the extinction spectrum.<sup>94</sup>

When now addressing the material-dependence of LSPR, let us recall that a plasmon is an electron-based phenomenon. Thus its properties strongly depend on the electronic structure (as described by the complex dielectric function) of the system within which it is excited. Theoretically, LSPR excitations are possible in any material possessing large negative real part and small imaginary part of the dielectric function (*e.g.* metals, alloys, and semiconductors). Gold and silver are the “classic” nanoplasmonic materials since they are the main systems chosen in LSPR studies due to their low losses in the visible frequency range. Hence, they exhibit strong and reasonably narrow LSPR peaks (**Figure 2.2**). Moreover their LSPR properties can be reasonably well explained by the Drude model in the vis-NIR range, *i.e.* below the interband transition threshold (2.4 eV for gold and 3.8 eV for silver, respectively<sup>95</sup>).

However, with increasing interest in LSPR and demands for applications in various fields, an increasing number of materials have been studied for their plasmonic properties. Thus, experimental reports on LSPR in, to name a few, Pt, Pd, Cu, Ni, Sn, Y and Al have become available.<sup>96–103</sup> Furthermore, alloys have also been considered for plasmonics, however only to a very limited extent. For example, it has been shown for the AuAg alloy nanoparticles that their LSPRs can be tuned to anywhere between that for pure Au nanoparticles to that of Ag nanoparticles by adjusting the alloy composition.<sup>104–106</sup> LSPR characteristics of some other alloy systems have also been demonstrated (*e.g.* AuCu<sup>107</sup> and AuFe<sup>108</sup>), however, only in a very limited fashion due to lack of versatile and reliable methods for fabricating alloy

nanoparticles. Lastly, a phase transformation of a material can also induce significant changes to LSPR since the transition changes the electronic structure and/or volume of the nanoparticles significantly. A prominent example is Pd when it is absorbing hydrogen (thus phase-transforms to palladium hydride), which leads to a considerable change in its electronic density of states due to weakened interactions between Pd atoms induced by interstitial hydrogen.<sup>109</sup>

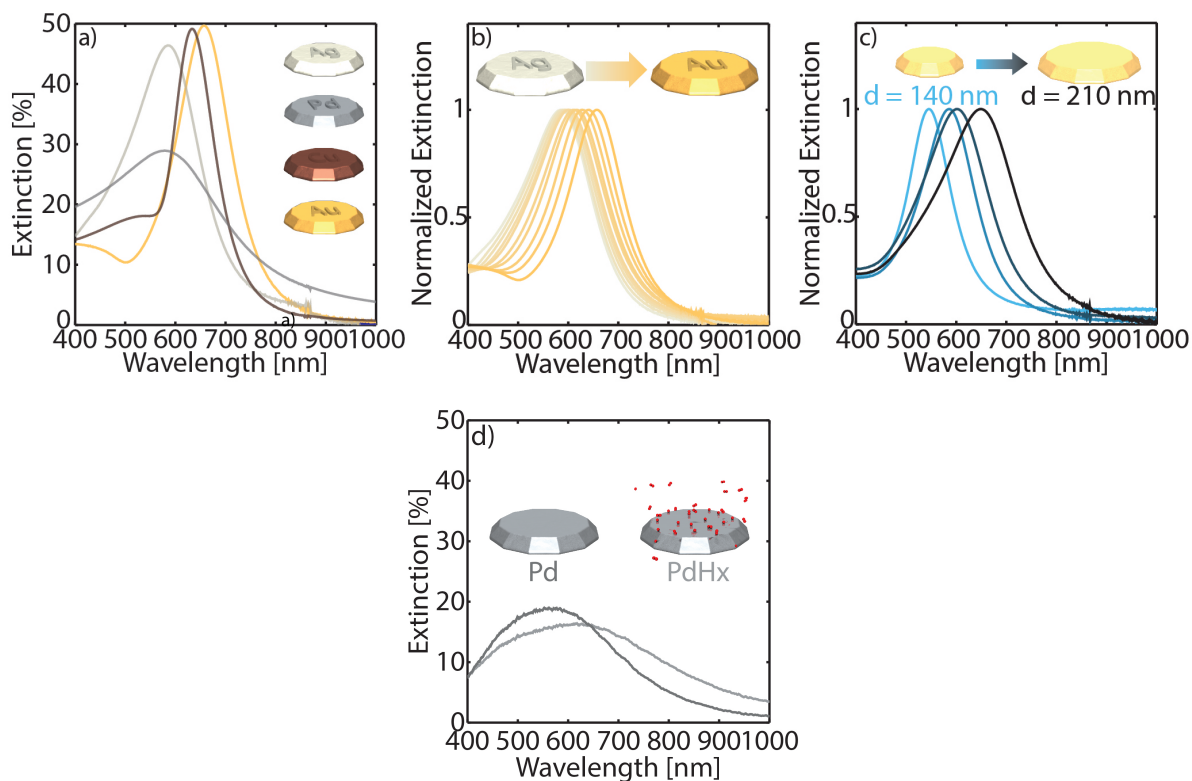


**Figure 2.3. The LSPR dependence on material, alloy composition and dimension.** (a) The different LSPRs exhibited by pure Ag, Pd, Cu and Au nanodisks with dimension of 190 nm diameter and 25 nm height. Note that the LSPR of Pd is much weaker and broader compared to the rest. (b) The evolution of LSPR for AuAg alloy nanodisks with different compositions (Au of 0–100 at. %, in 10 at. % steps). The dimensions are 190 nm diameter and 25 nm height. (c) The change in LSPRs in 50:50 AuAg alloy nanodisks with increasing diameter of 140 nm, 170 nm, 190 nm and 210 nm. The thicknesses are kept constant at 25 nm. (d) The change in LSPRs of Pd nanodisks with dimension of 190 nm diameter and 25 nm height when exposed to hydrogen, resulting in a palladium hydride, PdH<sub>x</sub>. Note that in panel (b) and (d) extinction is normalized.

In addition to the particle's size and material, the optical properties of plasmonic nanoparticles are also greatly influenced by their shape due to the polarizability's,  $\alpha(\omega)$ , shape dependency. Many works have been devoted to study the shape-LSPR relation both experimentally and theoretically. One of the fundamental works was done by Mock *et al.* in which they studied the spectra of silver nanoparticles with different shapes (spheres, triangles,

and cubes) but similar volume.<sup>110</sup> The study concluded that structures with shaper features have higher refractive index sensitivity (*i.e.* sensitivity towards the change in surrounding permittivity). The result was also supported by similar finding in other works.<sup>111,112</sup> In general, the deviation from the sphericity shifts the resonance towards larger wavelength due to higher concentration of charge and electric field at the sharp features.<sup>113,114</sup> Apart from the general shape of the particles, aspect ratio (*i.e.* ratio of width to height) also affects the resonance. High aspect ratio structures (shaped more like a one-dimensional structure) have longer resonance wavelength and higher intensity.<sup>113,115</sup> The reason for this property is the high charge accumulation in such structures, which leads to higher restoring force and consequently longer resonant wavelength.

**Figure 2.3** showcases the wide tunability of LSPRs achieved in this thesis by changing the plasmonic elements' composition and dimension.

## 2.3 LSPR Sensors

The LSPRs of nanoparticles are strongly dependent on many factors, as discussed in previous sections, *i.e.* shape, size, material and the dielectric function of the surrounding environment. Especially for the latter, if we recall equation 2.14 and use the fact that the refractive index,  $n$ , of a material is related to its dielectric function through  $\epsilon_d = n^2$ , we get

$$\lambda_{LSPR} = \lambda_p \sqrt{1 + 2n^2} \quad (2.17)$$

We see that the spectral position of the LSPR depends approximately linearly on the refractive index of the surrounding medium. This sensitivity, caused by the existence of the enhanced field in the vicinity of the plasmonic nanoparticles, makes it possible for LSPR to be used as a *sensor*; a nanoplasmonic sensor. The enhanced field can be considered to act as a *nanoscale probe* of events taking place very close to the plasmonic particle surface, within the volume of enhanced field. This constitutes a highly localized *sensing volume* that allows one to observe any change (*e.g.* adsorbate interaction, phase transition, etc.) occurring near the particle surface if such a change results in a modification of the local refractive index. **Figure 2.4** schematically illustrates the sensing volume for the case of a nanodisk in vacuum.

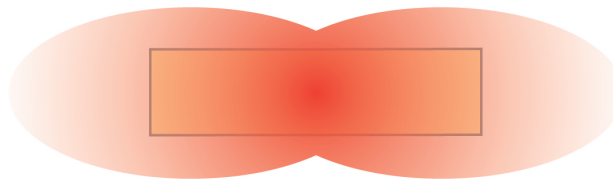


**Figure 2.4. Schematic illustration of the sensing volume around a plasmonic nanodisk.** The sensing volume (red areas) is created by the enhanced electromagnetic field surrounding a plasmonic entity. Within it local permittivity changes are detected as a spectral shift of the plasmonic peak.

A schematic illustration of an LSPR sensor, which detects changes in the permittivity in its vicinity, is shown in **Figure 2.5**. In this particular example, the binding of analyte molecules onto the particle increases the refractive index, which in turn alters the resonance condition of LSPR, causing it to red-shift.

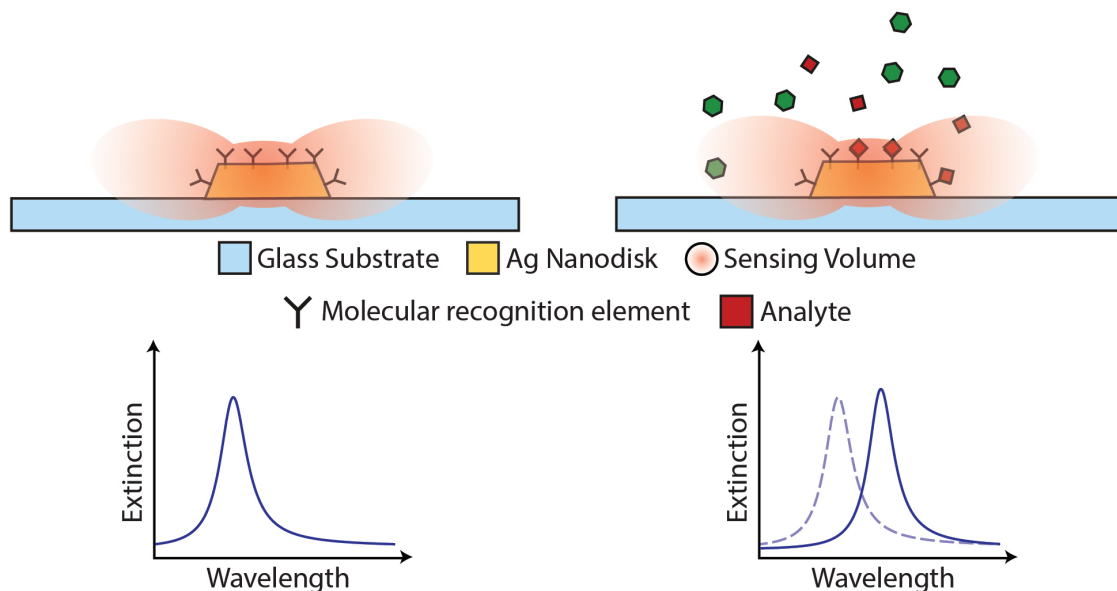


**Figure 2.5. Schematic illustration of an LSPR-based local refractive index sensor.** Analyte binding leads to higher refractive index in the vicinity of the nanoparticle. The increase in the refractive index is detected as a red-shift of the nanoparticle LSPR. The figure is adapted with modification from <sup>116</sup>.

**Figure 2.6** shows the three typical “fingerprints” of LSPR that all can be used as readout parameter of a nanoplasmonic sensing experiment, *i.e.* a change in peak position  $\lambda_{peak}$ , extinction at peak (*Ext @ Peak*), and full width at half maximum *FWHM*. They all have in common that they are the descriptor of a “physically meaningful” change of the LSPR effect. As described above,  $\lambda_{peak}$  is correlated with the resonance frequency. Furthermore, *Ext @ Peak* corresponds to the extinction cross section and the *FWHM* is characteristic for the damping/dephasing of the LSPR. Most often, all three readouts change simultaneously. However, one cannot say in general which one of these readouts gives the “best result” since they might be more sensitive to different aspects of the sensed process and thus relate to different physics. Therefore the readout parameter should be chosen carefully in order to get as good and as physically relevant signal as possible for the particular system studied. At the same time, the combination of different readout parameters may also provide deeper insight into the studied process at hand, compared to looking at one parameter alone.

The simple yet powerful concept of nanoplasmonic sensing has been proven to work impressively well, as shown by many examples reported in the scientific literature. So far, biosensors is by far the most exploited application area of nanoplasmonic sensing since it is label-free; thus it is very suitable for biological and biomedical assays.<sup>27</sup> The first report on surface-based LSPR biosensing was done by Englebienne in 1998.<sup>32</sup> Ever since, numerous

prototypes of LSPR refractive index sensors have been used to detect biological interactions including DNA-DNA,<sup>117</sup> carbohydrate-protein,<sup>118,119</sup> lipid-protein,<sup>120</sup> and protein-ligand binding.<sup>121–123</sup> Despite the vast number of applications developed in laboratories all over the world, quite few real devices have made it to the market so far. The ClearBlue pregnancy test kit developed by Unipatch in 1988 is one of the commercially available biosensors using plasmonic nanoparticles.

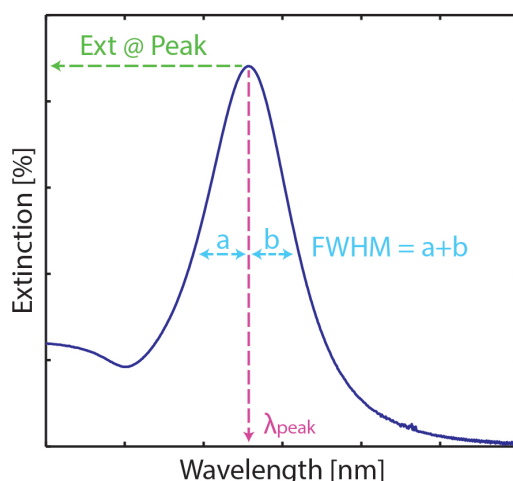


**Figure 2.6. The “fingerprints” of LSPR.** The LSPR extinction peak can be characterized by three physically relevant parameters:  $\lambda_{peak}$  (red arrow) denotes the wavelength where the peak occurs and thus denotes the resonance frequency of the plasmon. Extinction @ Peak (green arrow) shows the extinction value at  $\lambda_{peak}$  and denotes the extinction cross section. Lastly, the full width at half maximum (FWHM), depicted by the blue dashed line, characterizes the width of the peak taken at half of the maximum extinction value and corresponds to the lifetime of the plasmon in energy space. It is also common to define FWHM as twice the length of the fraction of the line width taken from the high energy (HE) and low energy (LE) side to the  $\lambda_{peak}$ , as marked by  $a$  and  $b$  respectively. Thus  $FWHM_{LE} = 2b$  and  $FWHM_{HE} = 2a$ .

Apart from the sensitivity of nanoplasmonic particles towards changes in their vicinity, they actually can also be used to study changes in their own intrinsic properties since LSPR is strongly dependent on shape, size, and material of the particles. Thus, any alteration to the plasmonic particles themselves either physically (e.g. shape and size) or chemically (i.e. phase change like oxidation, melting, hydride formation, etc.) affects the LSPR spectra, which means that such processes can be qualitatively (and quantitatively) observed by monitoring the corresponding changes in the LSPR spectra. The approach where the LSPR of the nanoparticle itself is used to monitor changes to the particle is usually called *direct plasmonic sensing* and was pioneered by our group.<sup>36</sup> In the past few years, this type of sensing has expanded the applicability of plasmonic sensing to the field of materials science. Examples of such studies include the hydride formation in palladium nanodisks,<sup>124</sup> oxidation of aluminum<sup>103</sup> and copper nanodisks<sup>101</sup> and freezing/melting of tin nanoparticles.<sup>100</sup>

The growing number of applications of nanoplasmonic sensors proves their versatility, which indeed is one of their greatest strengths. One reason is that the strong dependence of LSPR on size, shape and permittivity of the local surrounding offers practically viable possibilities to actively tune the sensor response to a wavelength of choice by engineering these parameters during the fabrication of the nanoparticles. This feature paired with ultra-high sensitivity makes it possible that very small amounts of analyte or even the tiniest changes in the sensor environment are enough to trigger the plasmonic signal. That said, the quest for “ultimate sensitivity” is still ongoing and many different nanoparticle designs have already been investigated.<sup>29</sup> This ranges from the simpler shapes, like disks,<sup>125</sup> to more complicated ones, like stars.<sup>126</sup>

Versatility is paired with additional advantages of nanoplasmonic sensing. For example, the method provides *in situ* measurement compatibility even in harsh environments, real-time and remote readout and the possibility of massive miniaturization and parallelization. The miniaturization can be forced down to single nanoparticles because even single plasmonic nanoparticles can be used as signal transducers in sensing experiments.<sup>127–129</sup> The parallelization opportunities come as a consequence of the small size of the signal transducer in nanoplasmonic sensors. A very large number of nanoparticles can be placed on the surface of the sensor chip and each and every one of them can, in principle, be tailored to *e.g.* specifically detect one type of molecule only. These extraordinary properties of nanoplasmonic sensing are universal. Thus one can take advantage of its abilities in other areas than biosensing; where it is mainly used currently. In fact, although growing, the number of applications of nanoplasmonic sensing outside the bio-related fields is still a lot smaller than the ones in bio-related fields.

As any technique, LSPR sensing also has its drawbacks and it is important to be aware of them. One of the main limitations is a direct consequence of one of the main advantages: the high sensitivity. In combination with the non-specificity of the readout (*i.e.* what is measured is a “shift” of a peak), this may lead to data which are complicated to interpret since different processes occurring simultaneously with/in the vicinity of the plasmonic particle all will give rise to a signal. As a consequence, it is very important to design experiments properly so that, ideally, conditions during measurement are such that the measured plasmonic signal originates entirely from the event of interest. Failing to do so results in the convolution of different signals.

As one ingredient for minimizing this problem, gold (and silver, which, however, easily oxidizes) is mainly used as plasmonic nanoparticle in sensing applications since it is non-reactive. Thus the possibility of signal coming from changes of the plasmonic nanoparticles themselves, *i.e.* oxidation, reaction with adsorbate or alloying with other metals, is minimized. Such effects can otherwise cause severe problems when measuring at elevated temperatures. Hence, in order to use LSPR sensors in more dynamic (*i.e.* under reactive gases and/or elevated temperature) environment, and thus broaden the applicability of LSPR sensors and make them more universal, these limitations must be overcome. Interestingly, one simple alternative has been developed in order to tackle some of those limitations and it will be discussed in the following section.

### 2.3.1 Indirect Nanoplasmonic Sensing (INPS)

A specific type of LSPR sensing is called Indirect Nanoplasmonic Sensing (INPS).<sup>76</sup> The key feature of the method is the use of thin dielectric layers, which can be deposited by either sputtering or chemical vapor deposition (CVD) methods (detailed explanation in **Chapter 4**). In INPS, such layers are applied to cover an array of plasmonic (usually Au or Ag) nanodisks in order to separate the optically active sensor nanodisks from the materials of interest, which are simply deposited on top of the dielectric layer. Therefore, the active plasmonic nanodisks are physically separated from and do not interact with the materials deposited onto the dielectric layer; thus the name *indirect* sensing. Despite the separation, the sensing functionality is still accessible since the enhanced LSPR field penetrates through the dielectric layer, which typically is only a few to ten nanometers thin. **Figure 2.7** shows a schematic depiction of the architecture of the INPS platform and its sensing principle.

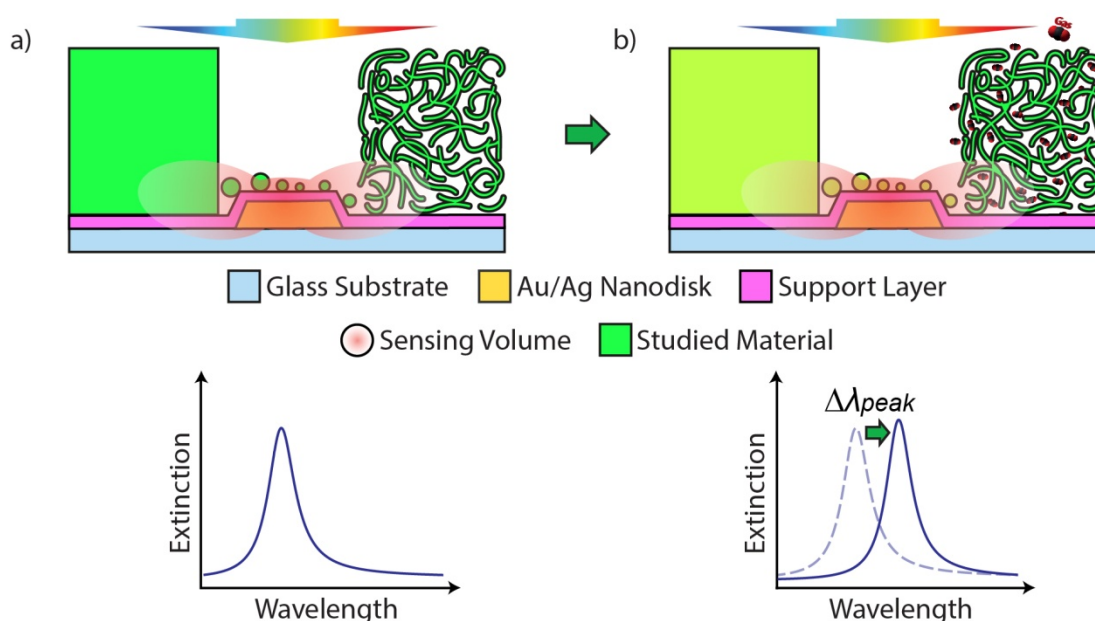


**Figure 2.7. Nanoarchitecture and sensing principle of indirect nanoplasmonic sensors.** A thin dielectric layer is deposited on the plasmonic (e.g. Au or Ag) nanodisk sensors to physically separate them from the nanomaterials to be studied. The latter can be small nanoparticles or thin films (solid or porous) and are simply deposited on top of the dielectric layer. Any change to the studied materials located within the sensing volume of the plasmonic nanodisks (e.g. phase transition, adsorption, rearrangement, etc.) is detected as change in the LSPR fingerprint parameters.

This simple addition of a dielectric layer, in fact, provides an efficient solution to some of the LSPR sensor shortcomings described above. For example it is able to contain the shape of the gold nanodisks even at high temperatures, and prevents contamination, alloying, or reaction of the gold nanodisks with the nano- or thin film materials being deposited on the sensor. Furthermore, the spacer layer can also be used to provide a tailored and homogeneous surface chemistry of the INPS sensor chip for a specific experiment, where it either can constitute an inert substrate for the nano- or thin film materials to be studied or participate actively in the process under study (**Figure 2.7**).

Since its invention in 2009, INPS has contributed to several important developments towards opening up the applicability of nanoplasmonic sensing to other than biosensing-related areas. In the original paper, three different applications were demonstrated to show the versatility of the platform: the glass transition temperature of confined non-conjugated polymers, the kinetics and thermodynamics of hydrogen storage in small Pd particles ( $< 5$  nm), and optical nanocalorimetry of hydrogen oxidation on a Pt nanocatalyst.<sup>76</sup> Further exploitation of INPS resulted in more focused applications in heterogeneous catalysis and materials science.<sup>36,130</sup> More recently, the platform has also been used to study the sintering of catalyst nanoparticles *in operando*.<sup>131–133</sup> Interestingly enough, another work has also successfully applied the sensing platform in solar cell technology where Gusak *et al.* used INPS sensors to study the diffusion of dye molecules in the dye-sensitized solar cell (DSSC) mesoporous titania photoelectrode.<sup>134</sup> The study demonstrated how INPS can be used to investigate diffusion and adsorption of molecules inside a porous material.

# 3 Hydrogen in Metals

Exactly 150 years ago, Thomas Graham, an English chemist, discovered that palladium could absorb a lot of hydrogen at ambient conditions. With his discovery, the foundation for a wealth of research on the fascinating metal-hydrogen interactions has been laid, and many applications of hydrogen in metals have been established and proposed since his pioneering study. In this chapter I will briefly discuss the general behaviour of hydrogen sorption in a metal, followed by discussing the specific application of metal-hydrogen interactions in hydrogen sensors.

## 3.1 Metal Hydrides

Being the smallest element in the universe, hydrogen atoms can occupy interstitial sites in many metal lattices to form stable compounds *i.e.* so-called hydrides. In some cases, the hydride formation process in a metal can happen spontaneously at ambient conditions, *i.e.* basically without activation barriers. In this case, hydrogen molecules ( $H_2$ ) adsorb on the metal surface and dissociate into hydrogen atoms (H), followed by subsequent diffusion into the interstitial sites in the metal lattice.

A simplified schematic picture of the hydride formation process in a metal at different stages is sketched in **Figure 3.1**. At low hydrogen partial pressures a solid solution of hydrogen in the host lattice is formed. This is called the  $\alpha$ -phase. In the  $\alpha$ -phase the attractive hydrogen-hydrogen interactions in the lattice are very weak since the amount of hydrogen is very low and thus the hydrogen atoms are far away from each other. Nonetheless, inclusion of hydrogen in interstitial lattice sites induces strain in the lattice of the host. As the hydrogen partial pressure is increased further the amount of hydrogen in the metal will also increase until a certain point where the attractive hydrogen-hydrogen interactions become appreciable due to more prominent lattice strain and electronic interactions. This causes hydrogen atoms to accumulate and form clusters (since this is energetically more favourable), eventually leading to the formation of domains where all sites are occupied. This is called the  $\beta$ -phase. The transition from  $\alpha$ -phase to  $\beta$ -phase is of first order. During the phase transition, the  $\alpha$ -phase and  $\beta$ -phase coexist in equilibrium and the growth of the  $\beta$ -phase occurs at the expense of the  $\alpha$ -phase. Eventually, the entire system is converted to  $\beta$ -phase and any further increase in hydrogen partial pressure will only result in minor changes in the hydrogen content in the hydride.<sup>135</sup>

A standard procedure to study the hydrogenation process in a metal is to map the hydrogen content in the host as a function of the hydrogen partial pressure at constant temperature; the so-called  $p$ - $C$  (pressure-composition) isotherms (**Figure 3.2a**). In the  $\alpha$ -phase, the hydrogen

content changes slowly with increasing hydrogen pressure. As the  $\beta$ -phase formation is started, there is a dramatic change in the hydrogen content in the metal over a very narrow pressure range. This region, where  $\alpha$ -phase and  $\beta$ -phase coexist, appears as plateau in the isotherm and is characterized by the “plateau pressure” in the middle of the plateau.

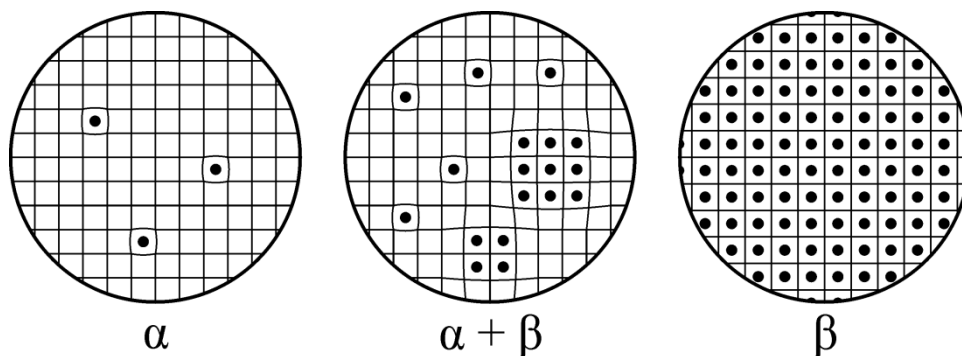


**Figure 3.1. Different stages during hydride formation/decomposition.** At low hydrogen partial pressures, few hydrogen atoms sit in interstitial lattice sites in the metal, constituting a solid solution called  $\alpha$ -phase. The hydrogen atoms locally strain the host lattice and the strain field created has relatively long range. Further increase of hydrogen pressure results in appreciable hydrogen-hydrogen interactions via these strain fields, which lead to the formation of nuclei of the hydride ( $\beta$ -phase) due to “clustering” of hydrogen atoms to reduce the total energy of the system. The growth of the  $\beta$ -phase continues until the entire metal is transformed to hydride. The figure is reproduced from <sup>136</sup> with kind permission.

If one reverses the process by reducing the hydrogen pressure to induce hydride decomposition, a similar process will occur with the only difference that the plateau pressure (*i.e.* when  $\beta$ -phase starts to decompose into  $\alpha$ -phase) will usually take place at lower hydrogen pressure compared to the one during hydride formation (see the dashed lines in **Figure 3.2a**). This *hysteresis* is a consequence of the lattice strain induced by the hydrogen presence in the metal lattice that causes volume expansion. The strain creates an energy barrier between the two phases that is different for hydride formation and decomposition and has to be surmounted for the formation or decomposition to occur by applying additional (higher or lower) pressure compared to the ideal strain-free lattice, in which no hysteresis would occur.

The equilibrium plateau pressures of a metal hydride system depend on the temperature the system is subjected to. Thus, by carrying out the  $p$ - $C$  measurements at different temperatures, one is able to construct the phase diagram for the considered metal-hydrogen system, as shown in **Figure 3.2a**. As the temperature increases, the plateau region (*i.e.* where  $\alpha$ -phase and  $\beta$ -phase coexist) and the hysteresis between hydride formation and decomposition continuously shrink until both features completely disappear above the so-called critical temperature ( $T_C$ ). Thus, for temperature higher than  $T_C$ , the transition from  $\alpha$ -phase to  $\beta$ -phase takes place continuously and reversibly when going the other way.

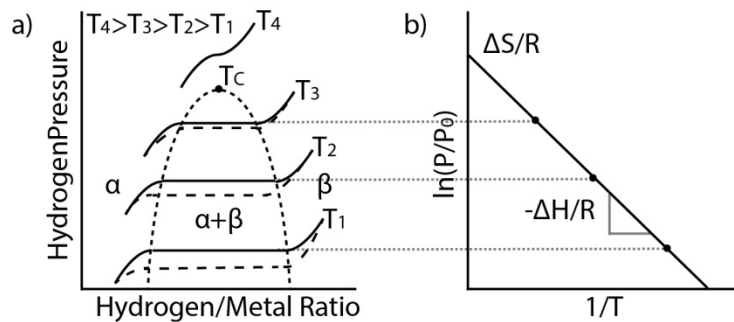


**Figure 3.2. Sketch of  $p$ - $C$  isotherms and the metal-hydrogen phase diagram.** (a) At constant temperature, in the simplest case of a binary hydride, there are three different phases;  $\alpha$ -phase at low hydrogen pressure, mixed  $\alpha$ -phase and  $\beta$ -phase region that occurs in a very narrow hydrogen pressure range (“plateau”) and the  $\beta$ -phase at the highest pressures. The equilibrium plateau pressure is temperature dependent and different equilibrium plateau pressures are exhibited for hydride formation and decomposition due to hysteresis. The width of the plateau and the width of the hysteresis shrink for higher temperatures until they eventually vanish at the critical temperature  $T_C$ . (b) Via van’ t Hoff analysis,  $\Delta H$  and  $\Delta S$  can be derived from the temperature dependence of the plateau pressure.

At the plateau pressure, equilibrium between the hydrogen in the gas phase and the hydride phase is achieved and thus the chemical potentials of hydrogen in the two phases are equal. From this equality arises the van’ t Hoff equation:

$$\ln\left(\frac{P}{P_0}\right) = \frac{-\Delta H}{RT} + \frac{\Delta S}{R} \quad (3.1)$$

where  $P$  is the plateau pressure,  $P_0$  is the atmospheric pressure (*i.e.* 1013 mbar)  $T$  is the temperature,  $R$  is the gas constant and  $\Delta H$  and  $\Delta S$  are the changes in enthalpy and entropy during the hydride formation, respectively. By plotting  $\ln(P/P_0)$  vs.  $1/T$ , if a straight line is obtained,  $\Delta H$  and  $\Delta S$  can be determined from the slope and intersection with the y-axis, respectively (**Figure 3.2b**). These parameters indicate the thermodynamic stability of the metal hydride and the change of entropy compared to hydrogen molecules in the gas phase.

The critical temperature,  $T_C$ , of a metal hydride system can be lowered or increased by material design. As mentioned earlier, the lattice strain induced by hydrogen atoms sitting in interstitial sites induces attractive interaction between the hydrogen atoms in the metal. However, it also creates an energy barrier (which thermally can’t be surmounted) that dictates the hysteresis between hydride formation and decomposition. Thus, for example by pre-straining the host lattice, *e.g.* by size reduction to the nanoscale or by alloying with other elements that strain the host lattice, it is possible to engineer the position of the plateau pressure and thus engineer both hysteresis and thermodynamics of the hydride. Shrinking hysteresis by reducing the particle size has been demonstrated by a number of works using palladium (Pd) with size less than 10 nm as the model system.<sup>137–140</sup> The effect comes from the fact that for smaller particle size, its surface to volume ratio is increased significantly.

Thus, surface tension plays a significant role for very small particles, affecting their hydrogen sorption properties.

Moreover, engineering  $T_C$ , hysteresis and thermodynamics of hydride formation can also be done by alloying the hydride-forming metal with another element. Again, for the well-studied Pd system, alloying with other elements such as Au, Ag and Ni has been shown to alter the position of  $T_C$ , as well as shrink the hysteresis.<sup>141–144</sup> In the case of Au and Ag as alloying element, both metals actually *expand* the host Pd lattice. Thus, the pre-strained lattice gives rise to a decrease in  $T_C$ , consequently lowering the plateau pressure during hydride formation and decomposition and decreasing the hysteresis between them. On the other hand, alloying Pd with Ni results in the opposite; a much higher  $T_C$ . This comes from the fact that Ni *contracts* the Pd lattice, which means that higher hydrogen pressure is required to initiate hydride formation.

## 3.2 Hydrogen Sensors

If we go back to the notion of a hydrogen economy previously discussed in **Chapter 1**, we can predict that the need for hydrogen sensors is about to increase significantly due to the imminent exploitation of hydrogen-powered technologies at a large scale. It is therefore of relevance to briefly discuss the state-of-the-art of hydrogen sensing technology.

Throughout the years, a variety of hydrogen sensors have been developed using diverse materials and transducing techniques such as mechanical, electric, thermal and optical.<sup>44</sup> The common criterion for the active sensing material used in these devices is that it, ideally selectively, reacts with hydrogen, which subsequently changes a measurable property of the material such as electrical or thermal conductivity, volume or optical contrast. For example metal oxide-based hydrogen sensors, which are widely used,<sup>44</sup> rely on a heated (*i.e.* 300–500 °C) semiconducting film under the presence of oxygen. Upon exposure to hydrogen, water will form on the surface of the film and subsequently donate electrons to it, thereby changing its electrical resistance, which is measured.

The ability of hydride-forming metals to dissociate and absorb hydrogen into their lattice makes them the second central class of materials used for hydrogen sensors,<sup>44,145</sup> along with other various applications such as hydrogen storage,<sup>146</sup> smart windows,<sup>147</sup> metal hydride batteries<sup>148</sup> and switchable windows.<sup>149</sup> In the development of such applications, especially for sensors, palladium (Pd) is the most common choice among the hydride-forming metals since it allows *barrierless* dissociation of hydrogen molecules on its surface at ambient conditions, and because it has the ability to absorb large amounts of atomic hydrogen into interstitial sites in its crystal lattice (up to 900 times its volume).<sup>150</sup> Due to these properties, in many of the hydrogen sensing applications, Pd is used as selective catalyst to dissociate the hydrogen molecules into hydrogen atoms, which later are “sensed” by other transducing techniques relying on another material. For optical sensors, however, Pd is typically not only used as selective catalyst for hydrogen dissociation but also as the main transducer material. This relies on the fact that Pd and its hydride, PdH<sub>x</sub>, exhibit significantly different optical

characteristics.<sup>151</sup> Therefore a significant number of optical hydrogen sensors based on Pd have been demonstrated.<sup>124,151,152</sup> As discussed in **Chapter 1**, optical sensors allow remote readout and, due to the fact that hydrogen is a flammable gas (at 4 vol. %), safer operation as they pose no risk of spark generation (in contrast with *e.g.* electrical sensors).

However, despite its apparent perfect suitability as active material in a hydrogen sensor, the applicability of Pd as transducer material for real applications is, in fact, quite limited. As mentioned in the previous section, hydride-forming metals exhibit an equilibrium plateau and significant hysteresis between hydride formation and decomposition. Pd is no exception, as seen in the isotherms shown in **Figure 3.3**. From the figure it becomes clear that Pd only shows a large response to a change in hydrogen pressure in its surrounding in a very narrow pressure range (*i.e.* around hydride formation and decomposition pressures). Moreover, the sensitivity at low pressure is most crucial when considering hydrogen leak sensors as hydrogen becomes flammable at 4 vol. % (*i.e.* 40 mbar). Thus pure Pd hydrogen sensors work well only if one needs to know if the hydrogen pressure has surpassed a certain pressure threshold (*i.e.* the plateau pressure). It is thus more suitable to be used as hydrogen *detector* rather than hydrogen sensor for continuous and real time monitoring of hydrogen concentration.

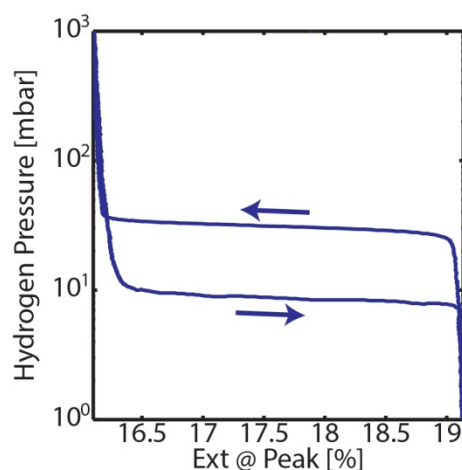


**Figure 3.3.** Hydride formation and decomposition isotherms of an array of Pd nanodisks with diameter of 190 nm and height of 25 nm. The isotherms were measured at 303 K and expressed using the Ext @ Peak readout of the Pd nanodisk LSPR (see **Chapter 2**). Note how the mixed phase regions (*i.e.* the plateaus) dominate the response, practically hindering accurate quantification outside those pressure ranges. The arrows point to the direction of the hydrogen pressure change.

The second problem of pure Pd-based hydrogen sensors is the hysteresis since it creates a large uncertainty in the sensor readout. This is due to the fact that the sensor signal not only will depend on the current hydrogen pressure (as desired), but also on the *history* of the hydrogen pressure, *i.e.* on which branch of the hysteresis loop the sensor is. However, for an accurate hydrogen sensor with wide operating range, a one-to-one relation between the hydrogen pressure and the sensor readout is critical.

As discussed previously, alloying hydride-forming metals with other elements may help alleviate the problem related to the hysteresis. In fact, alloy thin film optical sensors of PdAu, PdAg and PdNi have been demonstrated.<sup>141,143,144,153,154</sup> These sensors exhibit complete suppression of hysteresis for alloy compositions above a critical value (typically > 20 at. %) and also showcase higher sensitivities at low hydrogen pressures, and faster response time. Thus, they constitute a very promising platform to fulfil the stringent requirements for hydrogen sensors, as presented in **Table 1.1** in **Chapter 1**.

To push the performance of optical hydrogen sensors further, a platform beyond thin films is desired because thin film systems often suffer from degradation effects such as poor adhesion due to the inherent volume expansion during hydrogenation. To overcome this particular problem, *nanoparticulate* systems are very attractive. Furthermore, nanoparticulate systems offer attractive possibilities to engineer, for example, the sensor response time by tailoring the detection element dimensions. Also, we can capitalize one phenomena exclusively occurring at the nanoscale, such as the localized surface plasmon resonance (LSPR, previously discussed in **Chapter 2**), which may offer highly sensitive detection pathways, as well as unique potential for miniaturization and multiplexing.

To this end, in the recent years, numerous works on LSPR based hydrogen sensors have been published.<sup>145</sup> However, in all of these works, pure metals have been used as the transducer materials, and the related problems described above have not been addressed. As part of the reason for this state-of-the-art, we have identified the fact there are no reliable nanofabrication methods for *alloy* nanoparticles in controlled arrays on surfaces available. Thus, to date, alloy nanoparticles are almost exclusively produced via colloidal synthesis, which makes controlled integration of alloy nanoparticles on the surface of a solid-state device, as is required by most applications, very difficult. Therefore, the development of nanofabrication methods for the implementation of large area arrays of alloy nanoparticles on surfaces is imperative to advance the field of optical hydrogen sensors. The solution that I have developed is presented in **Paper I** and **Paper II**.

# 4 Nanofabrication

With “*nano*” preceding the word fabrication one should expect an unconventional and fascinating way of how nanofabrication works. Indeed, in the past few decades we have seen the establishment of nanofabrication that relies on various unique physical and/or chemical principles. It is these nanofabrication capabilities that have facilitated the unprecedented progress in nanoscience and nanotechnology. The work presented in this thesis is a direct consequence of and has been facilitated by state-of-the-art nanofabrication. All the sensors comprising plasmonic nanostructures developed and studied in my project were fabricated using a method called Hole-mask Colloidal Lithography (HCL).<sup>155</sup> There is a number of different thin film deposition and etching techniques involved in the HCL process. This chapter deals with the physics and concepts behind each of the used techniques (some of them are surprisingly simple!), their utilization, and their specific usage for the work included in this thesis. The chapter ends with a detailed discussion of the HCL process, and how it can be used to produce various nanostructures.

## 4.1 Spin Coating

Spin coating is one of the most common procedures for applying thin films to a flat surface and is used in a wide variety of industries and technology sectors. The advantage of spin coating is its ability to rapidly and easily produce very uniform films from a few nanometers to a few micrometers in thickness. Spin coating is mostly utilized to cast thin films of polymers from a solution.

Spin coating involves the rapid acceleration of a liquid “puddle” deposited on the substrate of choice, followed by high-speed rotation. The rotation spreads the solution/suspension evenly over the substrate to eventually form a uniform thin film on the entire substrate. The balance between the centrifugal force introduced by the rotation and the viscous force of the polymer solution, which is determined by the solution concentration, dictates the achieved film thickness. Of the many factors that seem to affect the obtained film thickness, only the spinning speed and solution viscosity actually do.<sup>156</sup> This promises a very reproducible technique to deposit thin polymer films. Spin coating is commonly followed by baking of the sample, *i.e.* the sample is heated on a hot plate or inside an oven to evaporate the excess solvent and thereby solidify the thin film. A schematic illustration of the general spin coating steps is depicted in **Figure 4.1**.

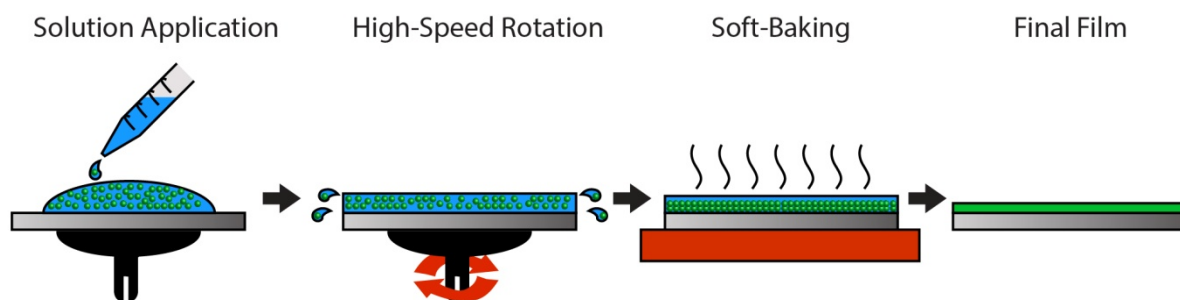


**Figure 4.1. Spin coating.** An excess of polymer solution is pipetted onto the substrate followed by high speed rotation, which induces centrifugal forces that throw excess solution off the edges to achieve a homogeneous film thickness. Soft baking is done to evaporate excess solvent to obtain a solid polymer film as the end result.

For the purpose of this thesis, spin coating is used as the first step of the hole-mask colloidal lithography (HCL) process to deposit a thin (~280 nm) PMMA polymer film. Moreover, I also used spin coating as the main procedure to deposit the studied polymer with microporosity, PIM-1, in **Paper III** and the polymer:fullerene blend, TQ1, PC<sub>61</sub>BM and PC<sub>71</sub>BM, in **Paper IV**.

## 4.2 Plasma Etching

Plasma is one of the (rather unfamiliar) states of matter along with gas, liquid, and solid. Plasma has very similar characteristics with gas (*i.e.* it does not hold any shape or volume unless contained) except that it consists of a *mixture* of electrons, ions, neutral atoms and molecules. The number of charge carriers in the plasma makes it electrically conductive and hence is strongly influenced by the presence of electromagnetic fields. These unique properties of plasma are what indeed define it as one of the states of matter. In short, plasma is an *ionized gas*.

Although plasma is in fact the most common state of matter in the universe, the natural occurrence of plasma is not very common on earth (as *e.g.* created by lightning) since it takes very special conditions and environment to keep plasma lasting. However, in the laboratory, plasma can be easily produced by applying high voltage to two electrodes with gas in between them. Due to the Coulomb force, the electrons and the atomic cores of the molecules in the gas are attracted to opposite electrodes; negatively charged electrons are forced towards the anode and positively charged ions towards the cathode. When the voltage is high enough the electrons and ions can be separated, creating “free” species that move towards the respective electrodes. These high-energy free electrons can, on their way towards the anode, collide with other atoms/molecules creating other ionized atoms/molecules and free electrons, which later induce more collisions and ionizations. This cycle of electrons breaking free creates a cascade of ionization giving rise to the formation of plasma.<sup>157</sup>

When building nanostructures, both addition and removal of material are mandatory steps required to achieve the desired designs. Interestingly, in nanofabrication, plasma can act as both agents. A term called *etching* is commonly used for the removal of materials in nanofabrication. When high-energy ions in a plasma hit a surface a transfer of energy occurs between the impinging ions and the atoms on the surface causing the atoms to be “kicked out”; a purely physical process defined as *sputter etching*.<sup>158</sup> On the other hand, one can also use a gas that chemically reacts with the materials and forms volatile products; a *chemical reactive ion etching* procedure,<sup>158</sup> see **Figure 4.2**. In this thesis chemical reactive ion etching is used to etch through the PMMA mask isotropically during the lithographic process. PMMA consists predominantly of carbon and hydrogen and it can therefore be reactively etched using oxygen plasma (*i.e.*  $O_2^+$ ) forming volatile  $CO$ ,  $CO_2$ , and  $H_2O$ . Additionally, short-time interaction of the plasma with the polymer surface has been reported to increase its hydrophilicity by changing its surface.<sup>159</sup> When polymers are exposed to oxygen they acquire the oxygen functionality in the form of hydroxyl, hydroperoxide, and carboxyl groups which have higher affinity towards water.<sup>160</sup>

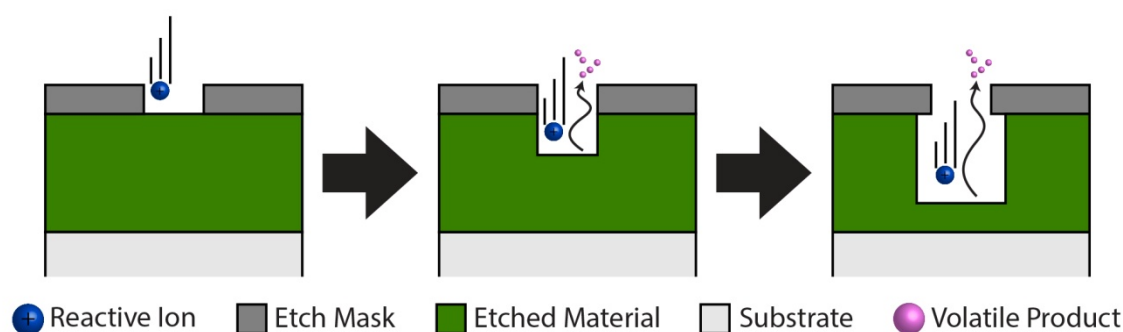


**Figure 4.2. Chemical plasma etching.** In a chemical etching process reactive-ions created in the plasma are accelerated towards a material and form volatile products. The process is highly one-directional and thus creates a high degree of isotropic etching. However, prolonged etching creates undercuts below the etch masks and thus the chosen etching duration should be carefully adjusted.

## 4.3 Thin Film Deposition

Deposition of thin films is one of the central processes in nanofabrication and a number of different methods exist for this purpose. In general, the techniques can be divided into physical or chemical deposition methods. Below, I give a brief overview of the deposition methods utilized within this thesis.

### 4.3.1 Physical Vapor Deposition

*Physical vapor deposition (PVD)* is based on the evaporation of the intended film materials by means of, as the name suggests, purely physical processes such as thermal evaporation and

sputtering, and is carried out in vacuum. The vapor of the desired material will condensate upon reaching the sample surface, which is placed above the evaporation source, and form a thin film (or small islands of particles, depending on the amount of material evaporated) while retaining its original composition. The vacuum environment used in the process is critical for the quality of the deposited films, as well as for the deposition process to occur at all. High vacuum provides longer mean free path for the vapor constituents created by heating or sputtering of the source/target. This is necessary to enable the vapor species to travel the long distance to the sample, as well as to reduce the probability of contamination of the grown film.

Vacuum evaporation uses a simple trick to create a material vapor: heating to high temperature. In fact, thermal evaporation of a solid offers a much higher vaporization rate as compared to other methods such as sputtering.<sup>161</sup> The way to heat the target material varies but the common methods are resistive and electron beam heating. In this work the latter has been used.

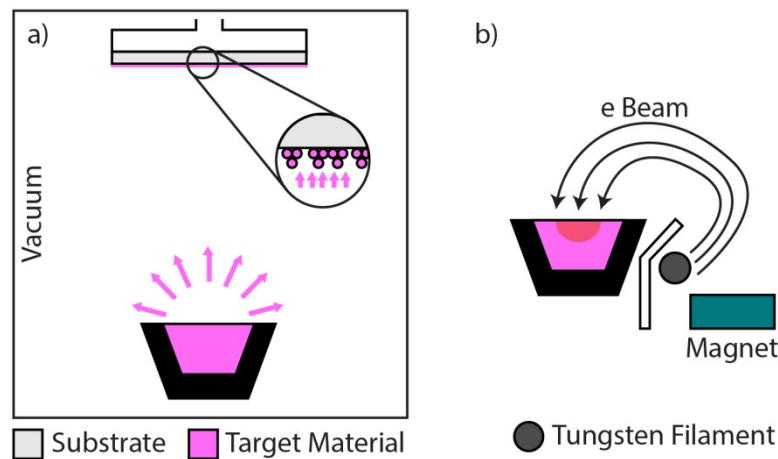


**Figure 4.3. Resistive and electron beam evaporation.** (a) Thin film deposition via evaporation relies on thermally vaporizing or sublimating a material to generate free atoms or cluster that travel towards a sample surface where they condensate into films. Vacuum conditions are required to minimize contamination and guarantee long enough mean free paths for the species to be able to reach the substrate, as well as for the vapor pressure above the source to be high enough for evaporation. (b) In electron beam evaporation a high DC voltage is applied to a tungsten filament that causes electrons to be discharged. These are then directed by the magnetic field towards the target material. The stream of electrons heats the target.

In the electron beam method the target material is heated by bombarding it with a beam of high-energy electrons discharged from a tungsten filament, as shown in **Figure 4.3**. The concept is similar to plasma etching explained in the previous section in terms of energy transfer. The transfer of momentum from the electrons of the beam directed onto the source material creates thermal energy, which then vaporizes the target. The advantage of electron beam evaporation over the resistive method is the ability to focus on a small spot to provide

much higher local heating. This provides both an extreme range of evaporation rate and the ability to vaporize materials with very high melting or sublimation temperature (e.g. tungsten, carbon, etc.).

The rate of deposition and the final film thickness is monitored using a QCM crystal. Current state-of-the-art evaporation systems allow control of the deposition at the sub-Ångström level. This assures a reliable and reproducible deposition at a very high level of accuracy and is thus an important feature when designing nanostructures with demanding precision on dimensions (see for example **Paper I**). In this thesis, electron beam deposition was used to deposit various metals (i.e. Au, Ag, Cu, Pd) to grow the plasmonic nanostructures.

### 4.3.2 Chemical Vapor Deposition

*Chemical vapor deposition (CVD)* relies on reactions of volatile compounds of materials to be deposited to produce a “new” solid (i.e. the reaction product) that condensates on the heated surface of a substrate. Naturally, the CVD process is subjected to thermodynamic and kinetic limitations, which makes it a generally more complex process than PVD. There are many factors that have to be precisely controlled in order to achieve the desired thin films, such as temperature, reactants, etc. The process is also constrained by the flow of gaseous reactants and products. A simple schematic illustration generally describing the CVD process is shown in **Figure 4.4**.

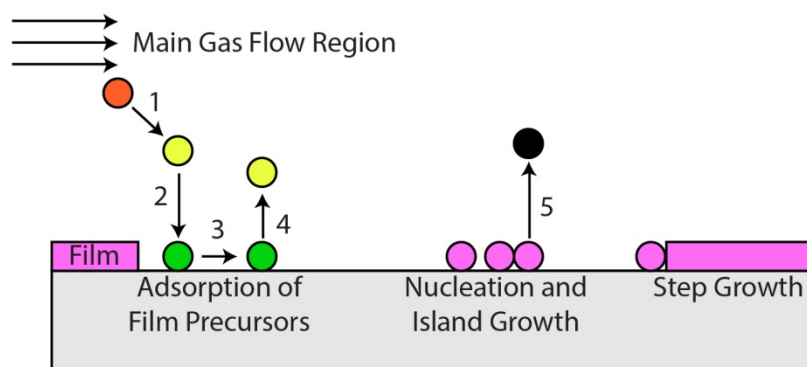


**Figure 4.4.** Sequence of gas transport and reaction processes contributing to CVD film growth. In CVD, the gas reactants are transported via diffusion to the reaction zone where they react chemically to produce new reactive species and by-products (1). Both types of species are then transported towards the surface (2) at which they chemi- or physisorb and diffuse (3) until a heterogeneous reaction, catalyzed by the surface, initiates and leads to the formation of the desired film. During the process there is also desorption of species (4) and by-products (5). They are, however, transported away from the surface by the flow from the reaction zone. Figure is adapted from <sup>162</sup>.

Despite the complexity, CVD is one of the most versatile deposition techniques known. It is able to deposit thin films for an impressive range of materials, i.e. semiconductors, dielectrics,

metallic films, refractory materials and ceramic fibres. Furthermore, CVD also features distinctive advantages over other deposition methods such as: (a) ability to produce highly dense and pure materials, (b) high deposition rates with relatively strong adhesion and good uniformity, (c) flexibility of controlling desired crystal structure, surface morphology, and orientation and (d) ability to coat complex-shaped structures with very good conformal coverage.<sup>162</sup> Point (a), (b), and, especially, (d) are factors that make CVD the main choice when a homogeneous coating of a corrugated surface is desired. Furthermore on point (d), different deposition techniques offer different characteristics of the formed films. As PVD is a very directional deposition method, it is not able to cover surfaces that are not facing the source. In contrast for CVD, the film is deposited wherever the gas reactants can get adsorbed on the surface. This particular distinctive signature outweighs the PVD process. A comparison between PVD and CVD is shown in **Figure 4.5**.

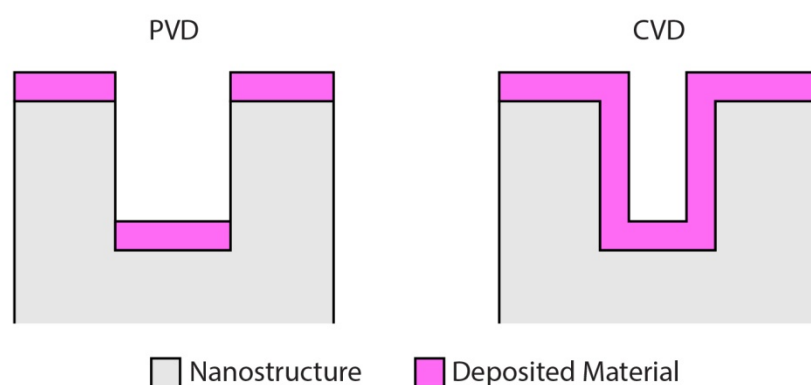


**Figure 4.5.** *The difference of achievable step-coverage between the PVD and CVD methods. PVD (left) is a directional deposition process. Surfaces parallel to the vapor trajectory cannot be covered, resulting in deposition only on surfaces facing the evaporation source. Hence PVD is a perfect choice whenever one wants to fabricate a structure based on mask-pattern transfer. On the other hand, CVD (right) depends on the volatile compound's diffusion (which ideally can go anywhere) so that the deposition covers all surfaces, creating very conformal coverage. Thus, CVD is very suitable for coating purpose.*

In this project silicon nitride ( $\text{Si}_3\text{N}_4$ ) was chosen as coating material to serve specific purposes: (i) as oxidation barrier to protect Ag nanodisks, as used in **Paper IV**, (ii) as a means to achieve homogeneous surface chemistry all over a plasmonic sensor surface, or both, and is an essential feature of the INPS platform.<sup>76</sup> Among many variants of CVD,<sup>162</sup> we used plasma-enhanced CVD (PE-CVD) which employs a plasma, along with the reactive gas, whose ions provide extra energy to initiate the endothermic process so that less heating is required. This is beneficial so that no major structural change as well as risk of oxidation occurs in the nanodisks when doing the deposition.

Silane ( $\text{SiH}_4$ ) gas is used as precursor following this reaction:



## 4.4 Hole-Mask Colloidal Lithography

With the background of some basic processes used in nanofabrication in place, we can now discuss the main fabrication technique I used to produce all plasmonic samples developed and utilized in this thesis, *i.e.* the Hole-mask Colloidal Lithography (HCL).<sup>155</sup> HCL is a variant of colloidal lithography and thus capable of creating amorphous arrays of nanostructures on large surface areas (cm<sup>2</sup> scale). The key feature of HCL is the usage of a sacrificial polymer layer as deposition hole-mask. This simple addition proves to be a very powerful aspect since HCL is able to produce a wealth of different types of nanostructures by simply depositing the desired materials through the mask.

**Figure 4.6** displays a schematic of the HCL process. Unless stated otherwise, later in the appended papers, all parameters regarding HCL fabrication are kept the same throughout the whole thesis as follows: Flat substrates, either borofloat glass, a silicon wafer or TEM windows, depending on the intended use, are cleaned (by sonication agitation for the case of glass and silicon substrate and only by rinsing for TEM windows in order not to break the membrane) in acetone, isopropyl alcohol (IPA), and deionized (DI) water, respectively, for three minutes each to remove organic contaminants. Prior to the self-assembly step, PMMA is spin coated (2000 rpm, 1 minute, produces thickness of roughly 280 nm) and soft-baked (170 °C, 10 minutes) (**Figure 4.6b**), and then ashed for 5 seconds in oxygen plasma (50 W, 250 Torr, 10 sccm) to increase hydrophilicity. This step is done in order to avoid spontaneous de-wetting during subsequent application of polyelectrolyte and colloidal particles. Subsequently, a thin layer of PDDA is applied onto the surface for 40 seconds and thereafter rinsed with DI water for 20 seconds and blown dry with N<sub>2</sub>. After this step, a monolayer of positively charged PDDA is adsorbed (**Figure 4.6c**). An aqueous suspension of oppositely charged polystyrene (PS) nanobeads is then pipetted onto the substrate and incubated for three minutes. PS particles will adsorb on the PDDA due to electrostatic forces at *ca.* 10% of a monolayer surface coverage. Electrostatic repulsion is also responsible for the self-assembled arrangement of PS particles. It prevents their aggregation and results in a pattern of particles with edge-to-edge distances on the order of one PS particle diameter or larger with no long-range order (**Figure 4.6d**). This step is followed by careful rinsing under DI water to remove the excess solution and N<sub>2</sub> blow drying. The latter helps to avoid rearrangement of the particles, which otherwise can be induced by capillary forces during drying. Fifteen nanometers of chromium are then thermally evaporated by electron beam evaporation (5 x E10<sup>-7</sup> Torr base pressure, 1 Å/s deposition rate) as a mask (**Figure 4.6e**). In this state the sample can be kept for long periods without any deterioration. The chromium-covered PS particles are then stripped away resulting in “holey” gold films with the hole diameter being defined by the PS particle size (**Figure 4.6f**). Subsequently, the samples are exposed to oxygen plasma etching (50 W, 250 Torr, 5 minutes, 10 sccm) (**Figure 4.6g**) leading to creation of the final hole-mask, which can be used to produce the desired nanostructures by simply depositing materials through it (**Figure 4.6h**).

An important feature of this method is that the evaporated materials will build up on top of the mask and at the rim of the holes in the mask, eventually causing the hole to shrink. This effect generates a tapered structure of the nanoparticles grown on the substrate through the hole of

the mask. However, with clever strategy, this feature can be utilized to create various complex arrangements of nanoparticles.<sup>163,164</sup>

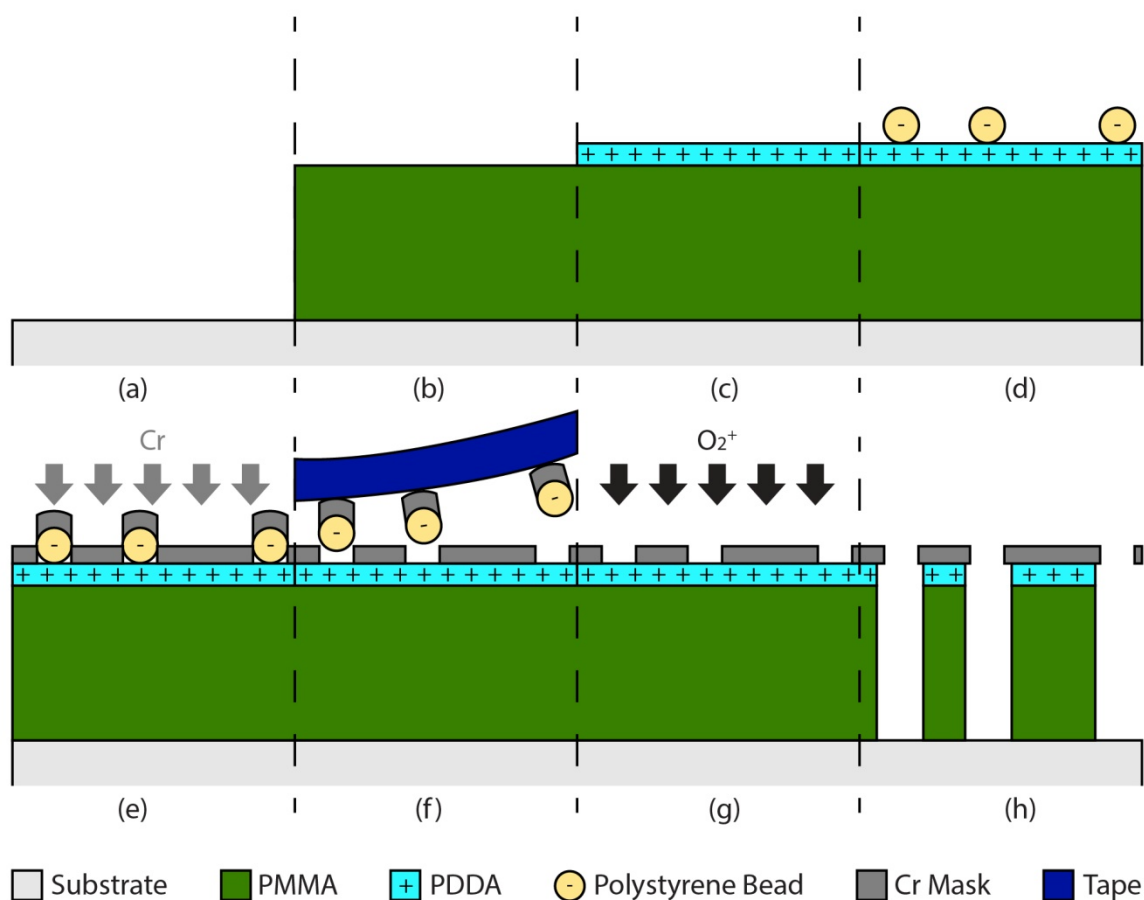


**Figure 4.6. Schematic depiction of the fabrication steps in Hole-mask Colloidal Lithography nanofabrication.** (a) A cleaned substrate, e.g. glass, silicon or TEM window, depending on the intended use, is the starting point. In steps (b) to (d) PMMA is deposited onto the substrate, followed by positively charged PDDA and negatively charged polystyrene particles, respectively. (e) Illustrates the chromium deposition to form the mask from the electrostatically self-assembled PS particles on the PMMA. Prior to the plasma etching in (g), the chromium-mask-covered PS particles are stripped away using tape (f), leaving an “unprotected” area of the PMMA, which later is etched all the way down to the substrate as shown in (h). At this step a deposition mask is created, which can be used to produce multiple nanostructure arrangements depending on the specifics of the final evaporation step.

#### 4.4.1 Nanodisk Structures

Once the evaporation mask has been produced by HCL it is straightforward to fabricate an array of nanodisks on a surface. The sample is loaded in an electron beam evaporation system and the material of choice is deposited through the hole-mask (**Figure 4.7a**). After the evaporation the sample is dipped in acetone. This dissolves the PMMA layer and removes the mask from the sample. After this process, commonly known as “liftoff”, only the nanostructures remain on the sample surface (**Figure 4.7b**).

As discussed before, the successive closing of the hole-mask during material deposition will create tapered structures with certain closing angle. This angle depends on the deposited material *e.g.* for Au, a closing angle of  $60^\circ$  has been reported.<sup>155,165</sup> An example of an array of Au nanodisks with diameter and height of 140 nm and 20 nm, respectively, fabricated by HCL is shown in **Figure 4.7c** and **d**. Note that a minor size variation exists for the fabricated nanodisks, which is caused by the intrinsic polydispersity of the PS beads used during the HCL process. In this thesis both Au and Ag nanodisks are used as plasmonic entities in **Paper III** and **Paper IV**, respectively. The choice was mainly made to tune the spectral position of the LSPR peak to avoid convolution with the absorption band of the polymers studied in the respective papers.

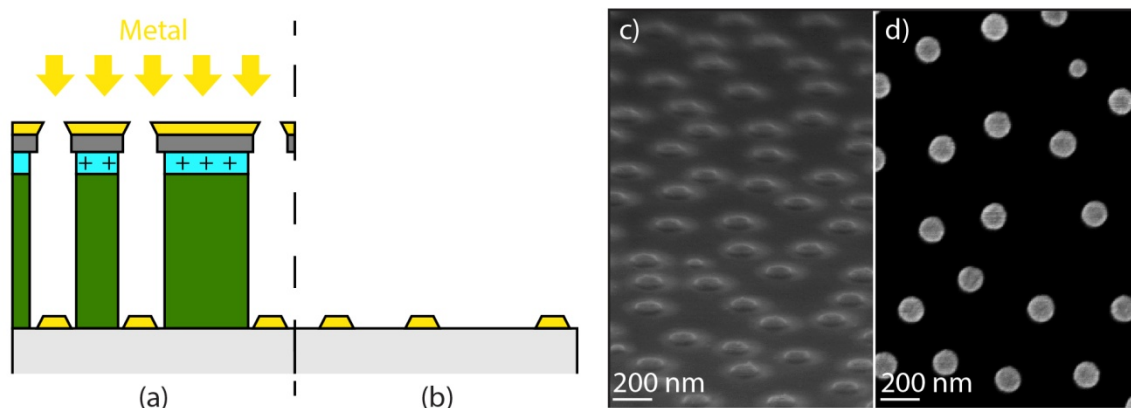


**Figure 4.7. Fabrication of nanodisks structures using HCL.** (a) PVD-deposition of the material through the mask. Due to the successive build-up of material on top of the mask and at the rim of the hole, the diameter of the hole shrinks gradually, creating a tapered structure inside the hole. (b) Removal of the PMMA mask is done by dissolving the PMMA resist layer in acetone, leaving only the nanodisks on the sample surface. (c)  $70^\circ$  tilt angle and (d) top-view SEM images of an array of gold nanodisks with mean diameter of 140 nm and height of 20 nm. Note the quasi-random arrangement of the nanodisks, as well as the slight polydispersity in size “inherited” from the polystyrene beads used during the fabrication to create the hole-mask.

#### 4.4.2 Layered Nanodisk Structures

In **Paper I** we establish a bottom-up fabrication strategy for arrays of metallic alloy nanodisks for use in nanoplasmonics and in plasmonic hydrogen sensing, as demonstrated in **Paper II**. The central idea behind the fabrication is to deposit layers of alloy constituents and anneal them to induce alloying. Fabrication of multilayer nanodisks is as straightforward as fabrication of nanodisks comprised of a single element discussed previously. The sample is loaded into an electron beam evaporation system with *different* sources. This allows successive deposition of the materials without taking the sample out. This makes the whole process more effective and also eliminates risk of contamination between the layers. As discussed before, the hole-closing of the HCL mask during deposition means that the diameter of the disk on top will be smaller than the one below. This should be considered when calculating the amount of material needed when designing certain alloy compositions.

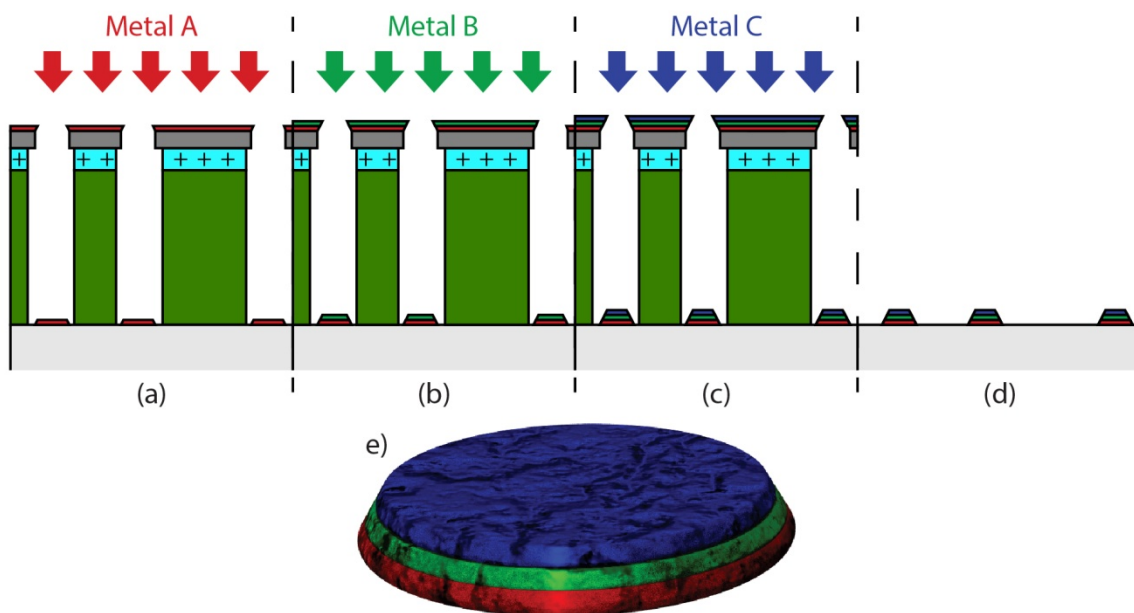


**Figure 4.8.** *Fabrication of stacked nanodisks with multiple metals using HCL. (a) to (c) show the successive deposition of different metals to form the layered nanodisks. The diameter of sequentially deposited disks shrinks due to the closing of the mask. (d) Removal of the PMMA mask leaves layered nanodisks on the substrate. (e) Schematic depiction of a layered nanodisk fabricated by successive depositions through a hole-mask.*

### 4.4.3 Indirect Nanoplasmonic Sensing Chips

Indirect nanoplasmonic sensing (INPS) samples are used in **Paper III** and **Paper IV**. The fabrication of this type of sample adds one more step to the fabrication of the nanodisk structures previously described. As mentioned before, INPS features a support layer to separate its active plasmonic sensing elements and the systems being probed. This is achieved by depositing a thin dielectric layer onto the plasmonic nanostructure arrays to form homogeneous sensor “chips”.

To ensure that a highly uniform and thus good protective layer is obtained (especially important in **Paper IV** as we went up to high temperature) I used a 10 nm  $\text{Si}_3\text{N}_4$  film grown by PE-CVD to coat the nanodisks (**Figure 4.9a**). This results in a conformal and uniform coating over the entire sample surface (typically  $1 \text{ cm}^2$ ), as shown schematically in **Figure 4.9b** and in the SEM images shown in **Figure 4.9c**.

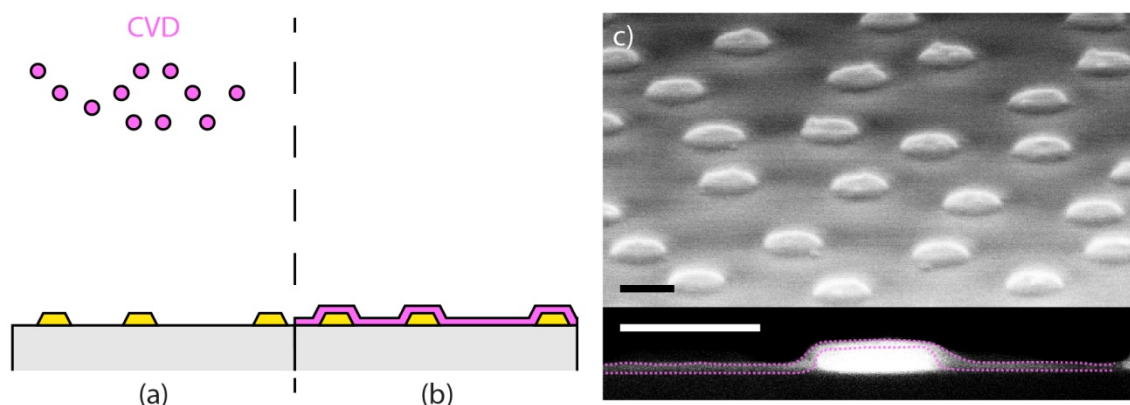


**Figure 4.9. Fabrication of Indirect Nanoplasmonic Sensing (INPS) chips using HCL.** (a) The homogeneous support layer is an essential part of the INPS chip and is obtained by deposition of a thin dielectric layer onto the plasmonic structures. PE-CVD is usually the method chosen due to its high quality and conformal coating ability. (b) Schematic depiction of an INPS sensor. (c)  $70^\circ$  (top) and  $90^\circ$  (bottom) tilt-angle SEM images of an INPS chip consisting of gold nanodisks with 190 nm diameter and 20 nm height, coated by a 10 nm  $\text{Si}_3\text{N}_4$  protective layer. Note the conformity of the coating (dashed lines). The scale bars are 200 nm.



# 5 Characterization Techniques

We never know how good something is until we see it and/or know what it is capable of. The same applies in science. Every sample should pass the process of characterization and this work is no exception. Naturally, in nanofabrication-related work, “appearance” is important. Thus the chapter begins with detailed information on how we can “see” nanoscale objects (even beyond what is on the surface) by two common electron microscopy methods, namely scanning electron microscopy and transmission electron microscopy. Later on in the chapter, I will introduce one of the main characterization techniques used in plasmonics-related studies, that is spectrophotometry. Basic spectrophotometry, as well as specific and detailed descriptions of the measurement setups used throughout the project are given. This includes a home-built vacuum chamber used to study the hydrogen absorption into alloy nanoparticles, and a quartz tube flow reactor to study the CO<sub>2</sub> adsorption energetics and glass transition temperature in polymer film systems.

## 5.1 Electron Microscopy

In the frame of nanoscale studies, the usage of *conventional* optical microscopy is limited. It is unable to image anything smaller than 100 nm as the diffraction limit comes into play. When the wavelength of light is larger than the samples’ features it will be diffracted and thus cannot be focused to a point<sup>166,167</sup> (however, a new methodology called near-field optical microscopy is able to break the far-field diffraction limit and successfully image a single molecule<sup>168</sup>).

To overcome this problem one needs to use radiation with substantially shorter wavelength. Electrons are the perfect choice. The wave-particle duality exhibited by electrons enables their usage as “light” in microscopy. There are two basic types of electron microscopy: transmission electron microscopy (TEM) and scanning electron microscopy (SEM).

### 5.1.1 Scanning Electron Microscopy

A scanning electron microscope (SEM) is a type of electron microscope that images a sample by scanning it with a beam of electrons in a raster scan pattern. Upon the bombardment, the electron beam-solid interactions produce various kinds of excitations as shown in **Figure 5.1**; secondary electrons, backscattered electrons, Auger electrons, as well as X-rays. These different excitations, which can be detected by a state-of-the-art SEM's different types of detectors and analyzers, stem from different processes and thus carry *different* information about the sample, *e.g.* topography, composition and electrical conductivity. As imaging modes are concerned, only secondary electron and backscattered electron signals contain information about topography. The two, however, originate from different process and have different energies. Thus they are captured using different detectors and carry slightly different information.

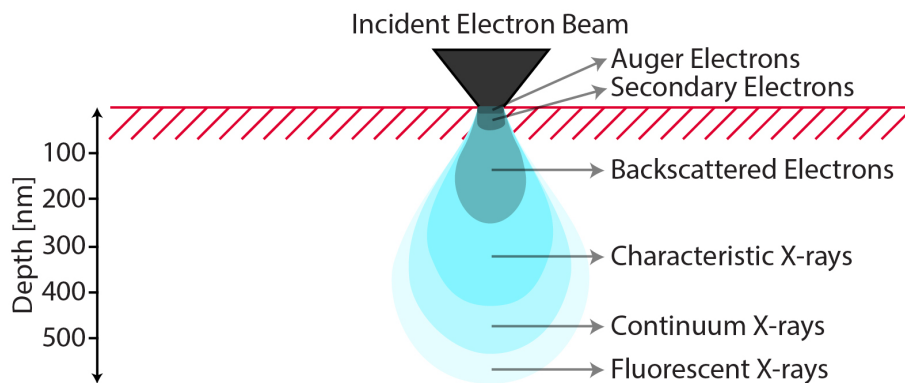


**Figure 5.1. Electron beam-solid interactions.** The electron beam penetrates into a solid in a teardrop-shaped feature creating various kinds of excitations. The depth where the excitations originate from depends on their energy; the shallowest (less than 5 nm), Auger electrons, have the lowest energy and the deepest (up to more than half micron), fluorescent x-rays, have highest energy. However, note that the penetration depth also depends proportionally on the primary electron beam energy. Secondary and backscattered electrons are commonly used for imaging, whereas characteristic X-rays are used to analyze the composition of a specimen.

Primary electrons, the electrons bombarding the sample, may lose some of their energy upon colliding and interacting with the sample. This process is known as inelastic scattering and occurs by interaction with electrons of the sample. From the principle of conservation of energy, the energy lost by the primary electrons will be compensated as a “gain” in energy of the electrons of the sample. If these are the outer-shell electrons, weakly bound to an atomic nucleus, most of the energy will be retained as kinetic energy, allowing the electrons to escape and travel through the solid as secondary electrons (SE). SE typically have kinetic energies of less than 100 eV and the average distance they can travel in the solid is limited to just one or two nm. This property provides excellent information about the surface structure as the secondary electrons that can be deflected have to be created very close to the surface.

Secondary electrons are thus able to produce the so-called topographical contrast of the samples studied.

Backscattered electrons (BSE), on the other hand, are elastically scattered primary electrons. Hence, backscattered electrons escape from the sample with energies only slightly smaller than the primary electron energy (*i.e.* higher energy than SE). Since elastic scattering is strongly dependent on the atomic mass of the atoms the electrons collide with, backscattered electron images can show contrast due to the different chemical composition of a sample; the so called composition contrast. The two can be used interchangeably in an SEM to obtain topographical information complemented with some compositional information.

As mentioned before, the interaction of primary electrons and the sample also creates the emission of X-rays resulting from electronic shell transitions in the sample (**Figure 5.1**). The emitted X-rays, which may originate from several microns deep within the sample, carry energy characteristics of the element emitted from (*i.e.* every element has its own set of characteristic peaks in its X-ray emission spectrum). Thus, detection and measurement of these energies permits quantitative elemental analysis known as energy dispersive X-ray spectroscopy (EDS).

SEM has been an invaluable tool for the work presented in this thesis. All samples used for SEM studies were fabricated on silicon substrate (rather than glass as used for all optical characterization) to minimize the effect of charging during imaging, which is heavily occurring on dielectric substrates. While the charging effect by itself is not damaging the sample, it nonetheless creates distorted and poor resolution images due to the built-up of electrons on the surface, creating an electric field, which in turn deflects the incoming electron beam in undesirable ways.

### 5.1.2 Transmission Electron Microscopy

In contrast to the SEM, the transmission electron microscope (TEM) shoots electrons through a very thin sample and is thus conceptually similar to a conventional optical microscope (but electrons are used instead of photons). Interactions of the electrons and the sample are reflected in the detected transmitted electrons, as well as in other emitted radiation such as X-rays. Similar to SEM, different type of information can be obtained depending on the sampled energy range and the type of analyzed radiation/electrons created upon interaction of the primary electrons with the specimen. In SEM, however, the resolution is mainly limited by the spot size of the scanning beam while in TEM is not. Hence, a far better resolution can be achieved in TEM (even to a single atomic column). However, TEM requires samples to be prepared in a special way since they have to be thin enough to allow electrons to be transmitted (~50 nm or ideally less). Thus a special TEM window or TEM grid type of sample support is required. In this thesis we used in-house made TEM windows following the procedure by Grant *et. al.*,<sup>169</sup> which consist of a 40 nm Si<sub>3</sub>N<sub>4</sub> thin film with 100 μm x 100 μm electron-transparent area (**Figure 5.2**).

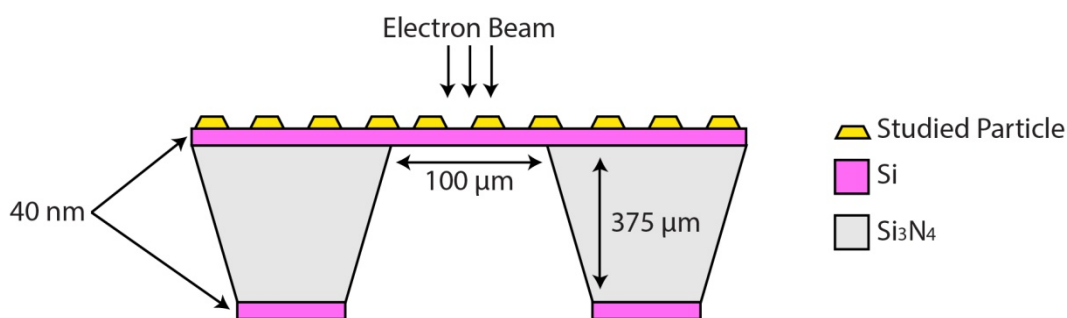


**Figure 5.2. Schematic of a TEM window used in this thesis.** The in-house made TEM windows consist of a 40 nm  $\text{Si}_3\text{N}_4$  thin film with  $100\ \mu\text{m} \times 100\ \mu\text{m}$  electron-transparent area. Note that the dimensions are not to scale. The figure is adapted from <sup>169</sup>.

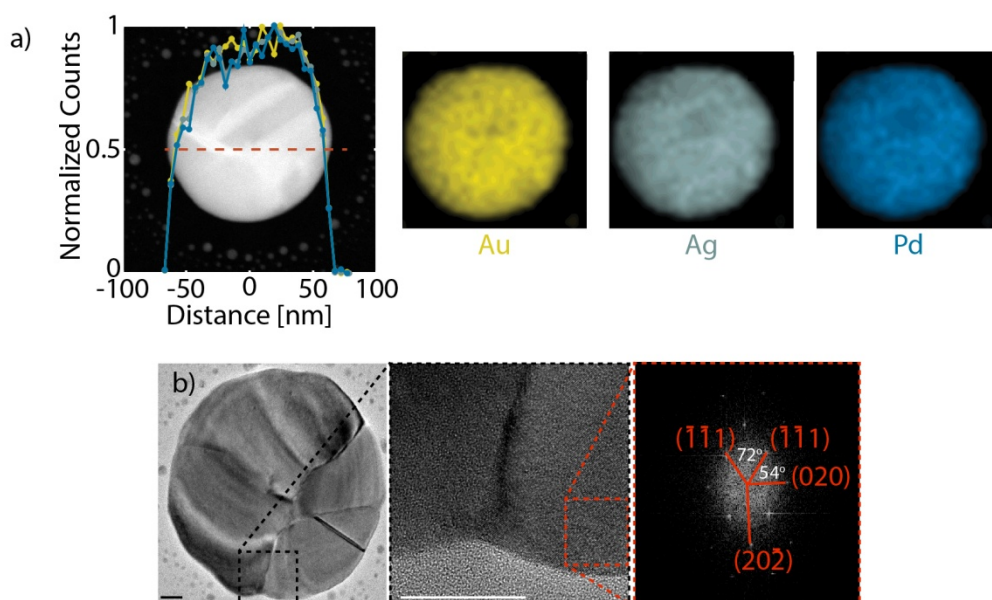


**Figure 5.3. TEM characterisation of nanofabricated alloy nanoparticles.** (a) Elemental distribution in a single ternary 33:34:33 AuAgPd alloy nanodisk is uncovered by an elemental linescan across a nanoparticle (left) and the corresponding elemental maps (right), using scanning TEM (STEM) EDS analysis. STEM analysis allows elemental scanning/mapping with 5 nm resolution and reveals homogeneous alloy distribution throughout the nanoparticle. (b) High resolution bright field TEM image that reveals impressive details on a single binary 70:30 AuPd alloy nanoparticle. For example, the polycrystallinity of the particle is clearly seen. Using electron diffraction and fast Fourier transformation (FFT), the crystallinity of different grains in the nanoparticle can be analyzed and lattice parameters/atomic spacing can be extracted (right).

For the purpose of the work presented in this thesis, TEM was used to characterize the elemental distribution and crystallinity of the alloy nanoparticles fabricated and applied in **Paper I** and **Paper II**. **Figure 5.3** shows a collage of different types of TEM-based analysis

used for characterization of my samples. The TEM analysis was carried out by our collaborators at the Center for Electron Nanoscopy at the Technical University of Denmark.

## 5.2 Optical Measurements

Since the sensors developed in this project rely on plasmonic effects, it is clear that the main characterization type should be one that is able to provide information about the optical properties of the samples. In my thesis, I relied mainly on spectrophotometry for this purpose. The basics of spectrophotometry and the instrument used to investigate the optical properties of my plasmonic samples at room temperature in air is explained first and is followed by a discussion of the instruments that allow spectrophotometry in special conditions, *e.g.* elevated temperature, controlled exposure of the sample to vapors and gases, etc.

### 5.2.1 Spectrophotometry

Spectrophotometry is a quantitative measurement of the optical properties of materials as a function of wavelength in the spectral region spanning from the ultraviolet (UV) to the visible (vis) and near-infrared (NIR) regions of the electromagnetic spectrum. In spectrophotometry the samples are irradiated by a beam of light which is either made monochromatic and scanned using a motorized grating or polychromatic upon irradiation and then analyzed using a fixed grating. Upon interaction with the sample its optical properties can be analyzed as a function of wavelength in both ways.

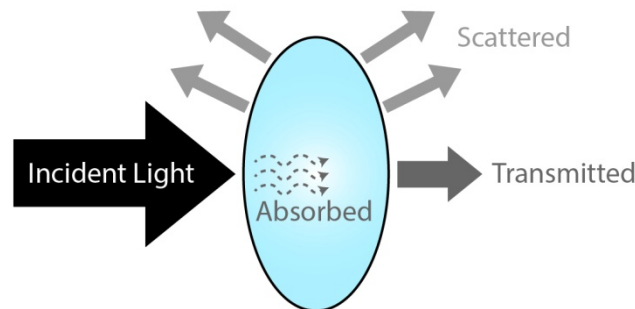


**Figure 5.4. Interaction of a material with an incoming plane wave.** When light is irradiated on a material it is transmitted, scattered, or absorbed. Transmitted light is defined as photons exiting the material in forward direction, whereas scattered light is elastically or inelastically deflected in other spatial directions. Absorbed light, however, “vanishes” as it is converted to other forms of energy in the material such as electronic excitations and, ultimately, heat.

When light is irradiated on an object it can be absorbed, scattered, or transmitted; as depicted in **Figure 5.4**. Transmittance ( $T$ ) is defined as the transmitted intensity ( $I$ ) compared to the incident light intensity ( $I_0$ )

$$T = \frac{I}{I_0} \quad (5.1)$$

Absorbance (*Abs*) is related to transmittance as

$$Abs = \log \frac{1}{T} = \log \frac{I_0}{I} \quad (5.2)$$

Scattering (*S*), on the other hand, is the part of the light emerging in different directions from the incident light and, together with absorption (*A*), related to the extinction (*E*), as described by the optical theorem, as

$$E = A + S \quad (5.3)$$

while

$$E = 1 - T \quad (5.4)$$

Hence, from equation 5.3

$$A + S + T = 1 \quad (5.5)$$

which makes up the total incident light intensity (**Figure 5.4**).

The wavelength-dependent extinction *E* of a sample can thus be determined by measuring the transmittance *T* and by comparing the difference between light that passes through the sample and a suitable reference (*e.g.* the bare substrate in my case).

In this work, a Varian Cary 5000 double-beam spectrophotometer, see **Figure 5.5**, has been used to measure the extinction *E* of all my samples under ambient conditions, *i.e.* no external heating or gas flow. It was mainly used for evaluating optical properties such as the effect of composition on the optical properties of plasmonic alloy nanodisk arrays in **Paper I**.

**Figure 5.6** shows a schematic drawing of a double-beam spectrophotometer. There are two light sources; a deuterium arc lamp for the UV and a halogen lamp for the vis-NIR region. The light then passes through the monochromator which, as the name suggests, separates the light spectrum into its individual wavelengths by step-wise adjusting its angle with respect to the incoming light. In the Varian Cary 5000 a diffraction grating is used as the monochromator. Once the spectrum is filtered out to the desired beam of a single wavelength, a chopper splits it into a sample and reference beam; hence the name double-beam spectrophotometer. The sample beam will pass through the sample whereas the reference beam travels parallel throughout the same environment except the sample. In order to produce reliable and reproducible measurements the light sources should produce stable intensity, *i.e.* no fluctuations. However, should the intensity fluctuate, which it always does in reality, the double-beam spectrophotometer ensures that both sample and reference beam fluctuate as well so that, in principle, the measurement will not be affected. Finally the light reaches the detector, which consists of a high performance multiplier tube for detection of the UV-vis and

a PbS photocell for the NIR region. The detector measures the intensity of the sample and reference beams alternately, and then compares their respective intensities to yield the fraction of light transmitted by the sample.

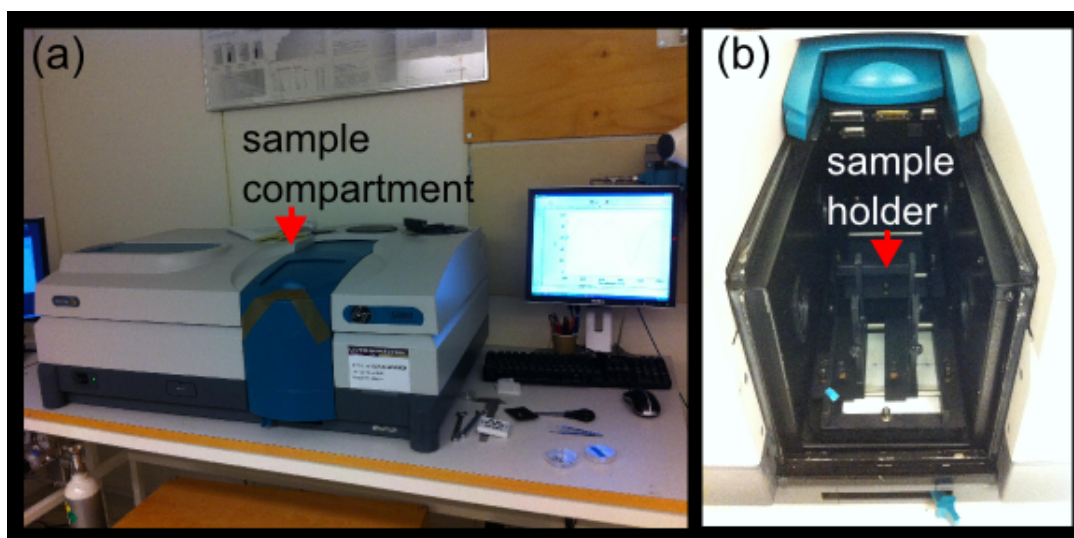


**Figure 5.5. Cary 5000 spectrophotometer.** (a) The overall appearance of the Cary 5000 spectrophotometer used for the optical characterization of my plasmonic nanostructures. (b) View into the sample compartment of the spectrophotometer.

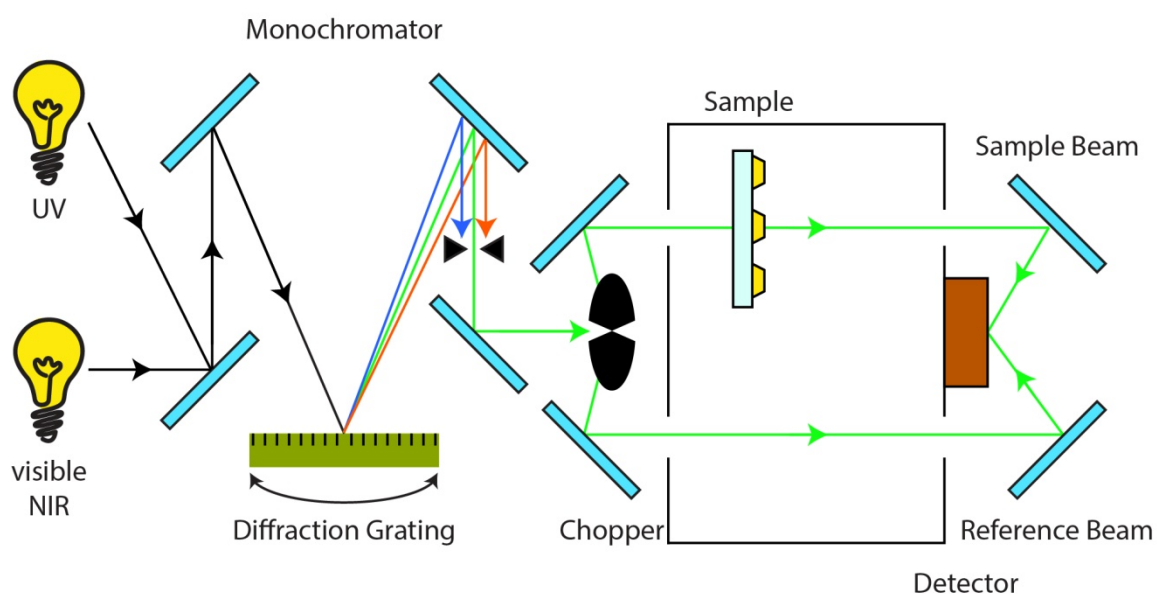


**Figure 5.6. Schematic of a double-beam UV-vis NIR spectrophotometer.** Two different light sources are used to produce UV and vis-NIR light. The diffraction grating acts as monochromator to transmit only the wavelength of interest to the sample. A chopper divides the beam into two paths: the sample beam which goes through the sample and the reference beam which travels the same path and environment except that it does not go through the sample. The detector then compares the two to eliminate effects like light source intensity fluctuations.

## 5.2.2 Optical Measurements in Temperature-Controlled Vacuum Chamber

For the purpose of thoroughly characterizing our alloy hydrogen sensors presented in **Paper I** and **Paper II**, a custom-built chamber was used (**Figure 5.7**). The setup is vacuum compatible and allows heating up to 100°C. The chamber, which consists of stainless steel, is also equipped with two sapphire glass windows to enable optical access to the sample. A fiber coupled from the window to a fixed-grating CMOS spectrophotometer measures the transmission through the sample, which is illuminated via a second fiber attached to the other side of the chamber.

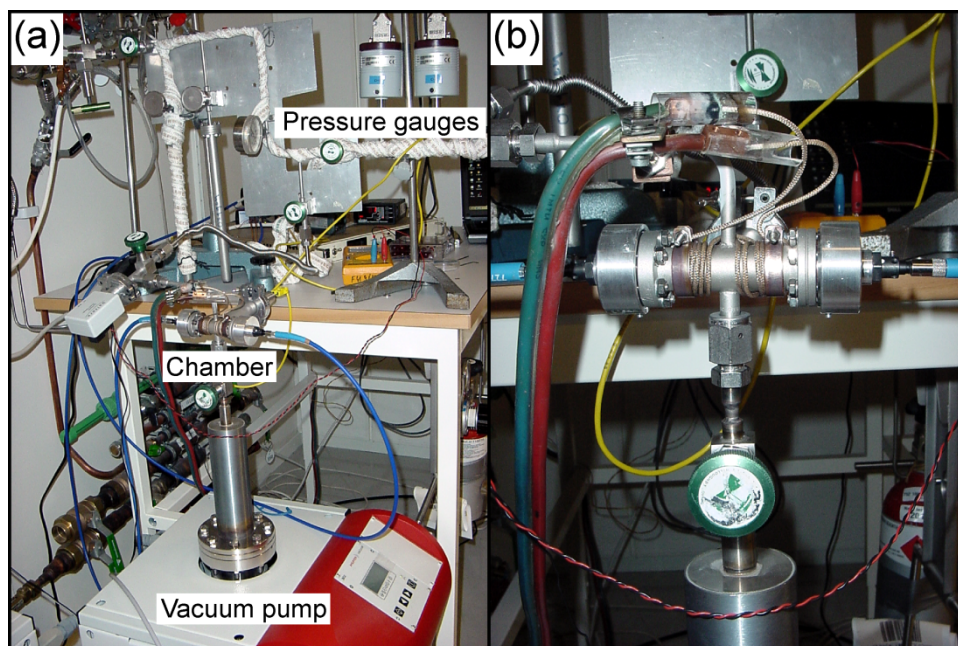


**Figure 5.7. Vacuum chamber used for hydrogen sensing measurements.** (a) Overview of the setup consisting of a measurement chamber where the plasmonic sensor is placed and various pressure gauges and a vacuum pump to control the hydrogen pressure in the chamber. (b) Close-up of the chamber. There are two fibers attached. One is coupled to a light source while the other is coupled to a spectrophotometer. The figure is reproduced from <sup>136</sup> with kind permission.

The setup is able to control the hydrogen pressure from a few microbar up to 1 bar, both quickly and (very) slowly. The former is important when assessing the kinetics of the studied system under hydrogen absorption/desorption. The latter allows careful study of the system under equilibrium conditions (*i.e.* sorption isotherms) at varying hydrogen pressure and is enabled by a UHV-compatible leak valve. The pressure inside the chamber is measured using a capacitance pressure gauge. The temperature is monitored using a thermocouple in direct contact with the sample, and it is controlled via a feedback mechanism by a Eurotherm controller and an external power supply used to control the heating via a resistive heating coil around the chamber. A Matlab program continuously records the sample temperature, the hydrogen pressure inside the chamber and the optical transmission through the sample.

### 5.2.3 Optical Measurements in Elevated Temperature under Gas Flow

In **Paper III** and **Paper IV** I investigated plasmonic sensors under exposure to specific gases and/or elevated temperatures. To perform this task, an Insplorion X1 mass flow reactor system (Insplorion AB, Göteborg, Sweden) was utilized. The general layout of the system is sketched in **Figure 5.8**. The reactor comprises a quartz tube equipped with a resistive heating coil. There are two thermocouples inside the tube; one to measure the upstream gas temperature and another one, touching the sample, to measure the actual temperature of the sample. The gas temperature reading is then used in a feedback loop to control the temperature in the reactor. Temperatures up to 600°C can be achieved. The sample is located in the middle of the tube, mounted on a stainless steel rod sample holder. To measure the optical properties of the samples, a fiber-coupled halogen lamp is used. A fixed-grating CMOS spectrometer then collects the transmitted light and yields the wavelength-resolved extinction spectra. Technically, the spectrometer is able to process the spectra as fast as every 1 ms. However, averaging is often employed to reduce noise. The gas composition and flow in the reactor are controlled by mass flow controllers, which are able to accurately supply sequences of different reactants flows and concentrations to the reactor tube and thus the sample.

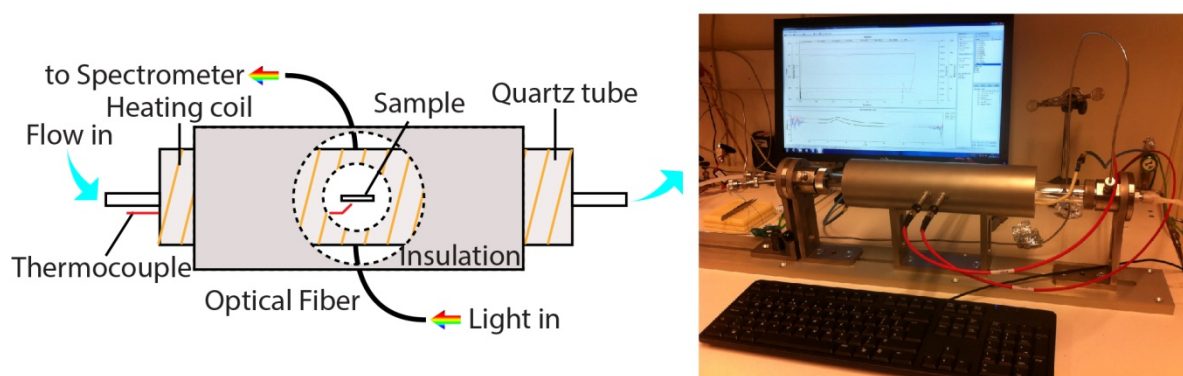


**Figure 5.8.** *Insplorion X1 catalytic flow reactor with optical access.* Left: A sketch of the reactor and optical readout. The sample is placed inside the quartz tube equipped with a resistive heating coil. Light is irradiated onto the sample via fiber optics and detected by a fiber-coupled fixed-grating CMOS spectrometer. The mass flow controllers allow accurate control of gas flow and composition. Right: Photo of the reactor.

### 5.2.4 Data Analysis

Once the spectra are acquired, the characteristic plasmonic readout parameters  $\lambda_{peak}$ ,  $Ext @ Peak$ , and  $FWHM$  are extracted using a MATLAB code, which fits a Lorentzian function to the spectra (available in the **Appendix**).  $\lambda_{peak}$  can be determined by finding the wavelength where the first derivative of the fit is zero.  $Ext @ Peak$  is then defined as the extinction value at the corresponding  $\lambda_{peak}$ .  $FWHM$  is determined by finding the point on the wavelength axis

(on the long wavelength side of the peak, to avoid convolution with *i.e.* interband absorption contributions or higher plasmonic modes) corresponding to the value of  $E = Ext @ Peak / 2$ . From this point, the spectral distance to the  $\lambda_{max}$  is calculated and multiplied by two to obtain the *FWHM*.

# 6 Summary and Outlook

**A**t this point, I hope the reader has acquired the necessary (and hopefully interesting) knowledge to understand the work presented in the appended papers of this thesis. In this chapter, I will give a brief summary for each of the papers, followed by a short outlook.

## 6.1 Summary of Appended Papers

In **Paper I** we established a bottom-up nanofabrication strategy to create arrays of metallic alloy nanoparticles on a support. This strategy is based on successive deposition of alloy element layers through a nanofabricated mask (HCL mask in our case) followed by annealing to induce the alloy formation. The method is generic as it allows any number of alloy elements to be mixed and is compatible with different types of nanolithography methods. We demonstrate this approach by fabricating Au-based binary alloy nanoparticles of AuAg, AuCu and AuPd and a ternary alloy of AuAgPd. We characterize the formed alloys using different electron microscopy techniques and reveal an astonishing control of alloy composition as well as homogeneous alloy formation throughout the fabricated nanoparticles. We also characterize the optical properties of the alloys and scrutinize the dependence of the LSPR characteristics on alloy composition. Finally, we demonstrate the anticipated application of alloy nanoparticles for plasmonic hydrogen sensing. Here we use a binary AuPd alloy with 30:70 at. % composition that shows complete suppression of hysteresis during hydrogen sorption.

**Paper II** constitutes a systematic assessment of AuPd alloy nanoparticles fabricated by the method presented in **Paper I** as plasmonic hydrogen sensors. We produce the alloy sensor nanostructures with Au concentrations ranging from 0–25 at. % (5 at. % steps) and investigate their hydrogen sensing properties. Similar to results from alloy thin films of the same system, we find continuous decrease of hysteresis upon increasing Au concentration until it completely disappears at 25 at. % Au. Consequently, this yields a plasmonic hydrogen sensor with readout accuracy better than 5 % throughout the investigated hydrogen pressure range of 1–1000 mbar. Moreover, we find an 8-fold sensitivity enhancement at low hydrogen pressure (*i.e.* 1–10 mbar) for sensors with 25 at. % Au compared to the one made of pure Pd, as well as reduced response time when exposed to 40 mbar hydrogen (*i.e.* the flammability limit). We also demonstrate a route to further improve the response time to below 1 second by tailoring the sensor nanoparticle size. All of the aforementioned results meet the performance targets for automotive hydrogen sensors previously presented in **Table 1.1**. Finally, we also find and

report a distinct wavelength-independence of the qualitative sensor response to hydrogen pressure. This opens the possibility to use single-wavelength plasmonic hydrogen sensing, which promises the use of low-cost optical components such as cheap LED light sources and a simple photodiode detector for implementation in real devices.

In **Paper III** we use indirect nanoplasmonic sensing (INPS) to study the CO<sub>2</sub> adsorption energetics of a microporous polymer. Specifically, we use the well-studied PIM-1 microporous polymer, which has high CO<sub>2</sub> permeability and selectivity, to benchmark our method. By tracking the LSPR readout of the PIM-1 coated INPS sensor in different CO<sub>2</sub> partial pressures and temperatures, we are able to construct CO<sub>2</sub> adsorption isotherms for PIM-1, and fit them using a Langmuir adsorption model. From the isotherms we extract a  $Q_{st}$  of around 29 kJ/mol, which is in excellent agreement with other reports measuring  $Q_{st}$  using conventional gravimetric analysis. One of the advantages of our method compared to traditional ones is that sample calibration (*i.e.* the determination of sample's mass and/or volume) is not necessary. We demonstrate this by obtaining similar  $Q_{st}$  from four PIM-1 samples with different thicknesses (300–600 nm) without the need to determine their masses and/or volumes accurately and involving them in the data analysis. Moreover, we find that the CO<sub>2</sub> adsorption on PIM-1 can be directly observed and characterized without using INPS (*i.e.* just on glass substrate) and similar  $Q_{st}$  were obtained. This is made possible since PIM-1 exhibits an optical absorption band below 480 nm, which provides the necessary optical contrast to detect CO<sub>2</sub> adsorption in a simple transmittance measurement. In summary, this study provides a general blueprint for efficient optical screening of (polymeric) materials in terms of their gas adsorption characteristics and energetics.

In **Paper IV** we utilize INPS to scrutinize the thickness-dependence of the glass transition temperature,  $T_g$ , of an organic solar cell absorber layer polymer:fullerene blend. Specifically, we investigate TQ1 as the donor polymer and the PC<sub>61</sub>BM:PC<sub>71</sub>BM fullerene mixture as acceptor. We investigate the  $T_g$  of pristine TQ1, of a 4:1 PC<sub>61</sub>BM:PC<sub>71</sub>BM mixture and of a 5:4:1 TQ1: PC<sub>61</sub>BM:PC<sub>71</sub>BM ternary blend, with thickness ranging from 20 nm to 350 nm. We find that the ternary blend displays a single  $T_g$ , which lies in between the  $T_g$  of its constituents. This proves that a finely mixed system was achieved. Moreover, all three systems exhibit distinct thickness dependence with increasing  $T_g$  for decreasing thickness. These trends are fitted with an empirical but well-established model, which results in fitting parameters that are in good agreement with the segmental lengths of the considered system and its constituents.

## 6.2 Outlook

There are many possibilities to continue the work presented in this thesis, especially since we successfully established a fabrication method to produce alloy nanoparticles with excellent control of their composition. I believe that this may promote significant progress in the field of “alloy plasmonics” both from a fundamental and practical point of view. For example, although it is not directly related to the work presented in this thesis, it will be interesting to

establish, if possible, a generic model of the dielectric function of metal alloys with arbitrary elements. Even for the well-studied AuAg alloy system, such a model is still actively sought after and several different approaches have been presented.<sup>104,170,171</sup> Finding such a generic model will be very important for designing alloy nanoparticles with desired optical properties, which later can be exploited for different applications.

For the hydrogen sensors, there are a lot of things that should be done to further optimize their performance, as well as to reach deeper understanding. For example, further increasing the Au concentration in the alloy; when does the hysteresis actually disappear and can we identify the critical point? Will adding even more Au to the alloy improve the sensor performance in terms of, for example, the response time? Alloying Pd with other metals such as Ag and Ni (and even use ternary alloys) and assess their performance are also viable actions when continuing the project. Furthermore, testing the sensors in more realistic environments is interesting and relevant. The first natural step in this direction should include a study in atmospheres containing other gases than pure hydrogen, *i.e.* O<sub>2</sub>, H<sub>2</sub>O and other species present at ambient conditions, *e.g.* CO which is known to poison Pd catalysts. To this end, to prevent sensor contamination by strongly binding species, the application of “protective” and H<sub>2</sub>-selective coatings is required, for example using metal organic frameworks (MOFs).<sup>172</sup> To explore this aspect with my nanoplasmonic sensors is thus a very interesting direction.

For INPS it will be very interesting to further develop the sensing structures themselves so that more information can be obtained. For example, a platform consisting of plasmonic disks with different dimensions so that they are spectrally detuned can be easily realised using HCL fabrication. There are two possibilities for these sensors. The first one is to arrange the disks on top of the other, separated by a dielectric layer. With enough separation by the dielectric layer, a plasmonically uncoupled system of two independent disks can be achieved. This arrangement could provide information about a material grown on the sensor surface at two different positions: one at the substrate interface and another one “inside” the material. This may provide valuable information about how a specific process may occur throughout a material. Another possibility is to have the two differently sized disks mixed in 2D arrays. In this arrangement, the size of the disks dictates the size of their sensing volume (as well as the spectral position of their resonances) with smaller disk exhibiting smaller sensing volume. Thus, a small disk is more sensitive at its surface while the bigger disks are more sensitive towards the bulk.<sup>173</sup> Using the complementary information obtained if two disk sizes are assessed simultaneously may therefore provide new means to obtain information about a material in their surrounding, such as thickness of an adsorbed layer.



# 7 Acknowledgements

This thesis would never have been written without all the helps and supports from *a lot* of wonderful people. Therefore I will never be able to mention all of these individuals in the following couple of pages but be assured that *all* helps are appreciated and remembered ☺.

My study has been financed by the Swedish Foundation for Strategic Research Framework Program RMA 11-0037.

First and foremost I would like to thank God for the life and His messengers for providing the light unto it. I sincerely hope that all the work done in this thesis (and beyond it) is of utmost beneficial for a lot of people.

I would also like to express my gratitude towards these people:

Christoph, simply for everything ☺. If I have to write down all of the good things that you have ever done to me it will be as thick as this thesis (and I am not exaggerating!). You are truly an inspiration and I would like to learn all from you. Please be prepared for the second half of my PhD as I may ask more and more questions!

Henrik, my examiner, for providing a comfortable working atmosphere, for all the feedbacks, and, more importantly, for your prompt help when my wife first came to Sweden. We owe you a lot.

Lasse, for all the helps in the lab. The upcoming year will be interesting for us.

Igor, for always being there answering my (kindergarten physics) questions. I learn a lot from you.

Ben and Jakob from DTU, for the very efficient and cool collaborations! I hope we have more coming in the future.

Chao and Niklas from Stockholm University, for the collaboration in the CO<sub>2</sub> project. Your attention to details is inspiring.

Camilla, Amaia and Christian, for the collaboration in polymer solar cells project. I really enjoy working with all of you.

Past and current members of Chemical Physics group. Thank you all for giving a nice environment to work in and all the fun activities. A special thanks to Carl who is now (enjoying life) in Japan. All the best for all of you!

Nanofabrication laboratory staffs, especially Henrik and Mats, who always help.

All of the Indonesian friends in Gothenburg that make it feel like home. Terima kasih!

My family in Indonesia, for all the loves, prayers and supports. I miss you all.

Lastly, for the ones who keep me “alive”, my angels. My wife Iie and my daughter Asiyah. Thank you for everything. I love you. All of these hardworks are dedicated to both of you.



# 8 Bibliography

- (1) Arnaiz-Villena, A.; Gomez-Prieto, P.; Ruiz-de-Valle, V. *Phylogeography of Finches and Sparrows*; Nova Science Publishers, 2009.
- (2) 1986: Coal mine canaries made redundant [http://news.bbc.co.uk/onthisday/hi/dates/stories/december/30/newsid\\_2547000/2547587.stm](http://news.bbc.co.uk/onthisday/hi/dates/stories/december/30/newsid_2547000/2547587.stm) (accessed Dec 10, 2015).
- (3) A canary in a coal mine <http://www.academia.dk/Blog/a-canary-in-a-coal-mine-in-the-19th-century-and/> (accessed Dec 10, 2015).
- (4) Feynmann, R. P. *Plenty of Room at the Bottom*, 1959.
- (5) Larsson, E. M.; Alegret, J.; Käll, M.; Sutherland, D. S. *Nano Lett.* **2007**, 7 (5), 1256–1263.
- (6) Electronic Sensors Market for Consumer by Product (Touch, Image, Motion, Temperature, Position, Pressure), Application (Entertainment, I.T., Communication Products, Home Appliances), & Geography (North America, Europe, APAC, ROW) - Worldwide Market Foreca <http://www.marketsandmarkets.com/Market-Reports/consumer-electronics-sensors-market-1293.html> (accessed Dec 10, 2015).
- (7) Sinclair, I. *Sensors and Transducers*, Third Edit.; Science Direct, 2001.
- (8) Kolmakov, A.; Zhang, Y.; Cheng, G.; Moskovits, M. *Adv. Mater.* **2003**, 15 (12), 997–1000.
- (9) Patolsky, F.; Zheng, G.; Lieber, C. M. *Nanomedicine (Lond)*. **2006**, 1 (1), 51–65.
- (10) Han, M.; Gao, X.; Su, J. Z.; Nie, S. *Nat. Biotechnol.* **2001**, 19 (7), 631–635.
- (11) Medintz, I. L.; Uyeda, H. T.; Goldman, E. R.; Mattoussi, H. *Nat. Mater.* **2005**, 4 (6), 435–446.
- (12) Li, J.; Lu, Y.; Ye, Q.; Cinke, M.; Han, J.; Meyyappan, M. *Nano Lett.* **2003**, 3 (7), 929–933.
- (13) Qi, P.; Vermesh, O.; Grecu, M.; Javey, A.; Wang, Q.; Dai, H.; Peng, S.; Cho, K. J. *Nano Lett.* **2003**, 3 (3), 347–351.
- (14) Shao, Y.; Wang, J.; Wu, H.; Liu, J.; Aksay, I. A.; Lin, Y. *Electroanalysis* **2010**, 22 (10), 1027–1036.

- (15) Schedin, F.; Geim, A. K.; Morozov, S. V.; Hill, E. W.; Blake, P.; Katsnelson, M. I.; Novoselov, K. S. *Nat. Mater.* **2007**, *6* (9), 652–655.
- (16) Barber, D. J.; Freestone, I. C. *Archaeometry* **1990**, *32* (1), 33–45.
- (17) The British Museum [www.britishmuseum.org](http://www.britishmuseum.org).
- (18) McMahon, S. J.; Currell, F. J. In *Nanomedicine*; Elsevier, 2013; pp 65–66.
- (19) Mie, G. *Ann. Phys.* **1908**, *330* (3), 377–445.
- (20) Stockman, M. *Phys. Rev. Lett.* **2004**, *93* (13), 137404.
- (21) Verhagen, E.; Kuipers, L.; Polman, A. *Nano Lett.* **2007**, *7* (2), 334–337.
- (22) Xiao, J. J.; Yakubo, K.; Yu, K. W. *Appl. Phys. Lett.* **2006**, *88* (24), 241111.
- (23) Smolyaninov, I. I.; Davis, C. C. *Chemphyschem* **2009**, *10* (4), 625–628.
- (24) Huang, X.; Jain, P. K.; El-Sayed, I. H.; El-Sayed, M. A. *Lasers Med. Sci.* **2008**, *23* (3), 217–228.
- (25) Hainfeld, J. F.; Slatkin, D. N.; Smilowitz, H. M. *Phys. Med. Biol.* **2004**, *49* (18), 309–315.
- (26) Paciotti, G. F.; Kingston, D. G. I.; Tamarkin, L. *Drug Dev. Res.* **2006**, *67* (1), 47–54.
- (27) Anker, J. N.; Hall, W. P.; Lyandres, O.; Shah, N. C.; Zhao, J.; Van Duyne, R. P. *Nat. Mater.* **2008**, *7* (6), 442–453.
- (28) Novo, C.; Funston, A. M.; Mulvaney, P. *Nat. Nanotechnol.* **2008**, *3* (10), 598–602.
- (29) Stewart, M. E.; Anderton, C. R.; Thompson, L. B.; Maria, J.; Gray, S. K.; Rogers, J. A.; Nuzzo, R. G. *Chem. Rev.* **2008**, *108* (2), 494–521.
- (30) Mayer, K. M.; Hafner, J. H. *Chem. Rev.* **2011**, *111* (6), 3828–3857.
- (31) Garcia, M. A. *J. Phys. D: Appl. Phys.* **2011**, *44* (28), 283001.
- (32) Englebienne, P. *Analyst* **1998**, *123* (7), 1599–1603.
- (33) Tittl, A.; Giessen, H.; Liu, N. *Nanophotonics* **2014**, *3* (3), 157–180.
- (34) Kreno, L. E.; Hupp, J. T.; Van Duyne, R. P. *Anal. Chem.* **2010**, *82* (19), 8042–8046.
- (35) Nugroho, F. A. A.; Xu, C.; Hedin, N.; Langhammer, C. *Anal. Chem.* **2015**, *87* (20), 10161–10165.
- (36) Larsson, E. M.; Syrenova, S.; Langhammer, C. *Nanophotonics* **2012**, *1* (3-4), 249–266.

- (37) Global Challenges for Humanity <http://www.millennium-project.org/millennium/challenges.html> (accessed Dec 12, 2015).
- (38) Lacis, A. A.; Schmidt, G. A.; Rind, D.; Ruedy, R. A. *Science* **2010**, *330* (6002), 356–359.
- (39) Schlapbach, L. *Nature* **2009**, *460* (7257), 809–811.
- (40) Bockris, J. O. M. *Energy, the solar hydrogen alternative*; Wiley: New York, 1975.
- (41) Flat Icon [www.flaticon.com](http://www.flaticon.com).
- (42) HD Wallpapers Act [www.hdwallpapersact.com](http://www.hdwallpapersact.com).
- (43) Boon-Brett, L.; Bousek, J.; Black, G.; Moretto, P.; Castello, P.; Hübert, T.; Banach, U. *Int. J. Hydrogen Energy* **2010**, *35* (1), 373–384.
- (44) Gupta, R. B. *Hydrogen fuel: production, transport and storage*; Taylor & Francis, 2009.
- (45) Contribution of Working Group III to the Fifth Assessment Report of the Intergovernmental Panel on Climate Change. <https://www.ipcc.ch/report/ar5/wg3/> (accessed Dec 11, 2015).
- (46) Turino, G. M.; Goldring, R. M.; Heinemann, H. O. Nahas, G., Schaefer, K. E., Eds.; Springer-Verlag: New York; pp 273–281.
- (47) Poyart, C. F.; Nahas, G. G.; Vulliemoz, Y. *Mol. Pharmacol.* **1968**, *4* (4), 389–401.
- (48) D’Alessandro, D. M.; Smit, B.; Long, J. R. *Angew. Chem. Int. Ed. Engl.* **2010**, *49* (35), 6058–6082.
- (49) Gibbins, J.; Chalmers, H. *Energy Policy* **2008**, *36* (12), 4317–4322.
- (50) Sumida, K.; Rogow, D. L.; Mason, J. A.; McDonald, T. M.; Bloch, E. D.; Herm, Z. R.; Bae, T.-H.; Long, J. R. *Chem. Rev.* **2012**, *112* (2), 724–781.
- (51) Choi, S.; Drese, J. H.; Jones, C. W. *ChemSusChem* **2009**, *2* (9), 796–854.
- (52) Bae, Y.-S.; Snurr, R. Q. *Angew. Chem. Int. Ed. Engl.* **2011**, *50* (49), 11586–11596.
- (53) Farha, O. K.; Eryazici, I.; Jeong, N. C.; Hauser, B. G.; Wilmer, C. E.; Sarjeant, A. A.; Snurr, R. Q.; Nguyen, S. T.; Yazaydin, A. Ö.; Hupp, J. T. *J. Am. Chem. Soc.* **2012**, *134* (36), 15016–15021.
- (54) Nugent, P.; Belmabkhout, Y.; Burd, S. D.; Cairns, A. J.; Luebke, R.; Forrest, K.; Pham, T.; Ma, S.; Space, B.; Wojtas, L.; Eddaoudi, M.; Zaworotko, M. J. *Nature* **2013**, *495* (7439), 80–84.
- (55) Keller, J. U.; Robens, E.; du Fresne von Hohenesche, C. *Characterization of Porous Solids VI, Proceedings of the 6th International Symposium on the Characterization of*

- Porous Solids (COPS-VI)*; Studies in Surface Science and Catalysis; Elsevier, 2002; Vol. 144.
- (56) Keller, J. U.; Rave, H.; Staudt, R. *Macromol. Chem. Phys.* **1999**, *200* (10), 2269–2275.
- (57) Grimes, C.; Varghese, O.; Ranjan, S. Springer, 2008.
- (58) Global Market Outlook - For Photovoltaics 2013-2017 <http://www.fotovoltaica.com/fv-look.pdf> (accessed Dec 11, 2015).
- (59) Top 20 Most Efficient Solar Panels on the Market <http://sroeco.com/solar/top-20-efficient-solar-panels-on-the-market/> (accessed Dec 11, 2015).
- (60) Liu, Y.; Zhao, J.; Li, Z.; Mu, C.; Ma, W.; Hu, H.; Jiang, K.; Lin, H.; Ade, H.; Yan, H. *Nat. Commun.* **2014**, *5*, 5293.
- (61) Dang, M. T.; Hirsch, L.; Wantz, G. *Adv. Mater.* **2011**, *23* (31), 3597–3602.
- (62) Müller, C. *Chem. Mater.* **2015**, *27* (8), 2740–2754.
- (63) Bergqvist, J.; Lindqvist, C.; Bäcke, O.; Ma, Z.; Tang, Z.; Tress, W.; Gustafsson, S.; Wang, E.; Olsson, E.; Andersson, M. R.; Inganäs, O.; Müller, C. *J. Mater. Chem. A* **2014**, *2* (17), 6146–6152.
- (64) Lindqvist, C.; Sanz-Velasco, A.; Wang, E.; Bäcke, O.; Gustafsson, S.; Olsson, E.; Andersson, M. R.; Müller, C. *J. Mater. Chem. A* **2013**, *1* (24), 7174.
- (65) Bertho, S.; Haeldermans, I.; Swinnen, A.; Moons, W.; Martens, T.; Lutsen, L.; Vanderzande, D.; Manca, J.; Senes, A.; Bonfiglio, A. *Sol. Energy Mater. Sol. Cells* **2007**, *91* (5), 385–389.
- (66) Yang, X.; van Duren, J. K. J.; Janssen, R. A. J.; Michels, M. A. J.; Loos, J. *Macromolecules* **2004**, *37* (6), 2151–2158.
- (67) Forrest, J. A.; Dalnoki-Veress, K.; Dutcher, J. R. *Phys. Rev. E* **1997**, *56* (5), 5705–5716.
- (68) Forrest, J.; Dalnoki-Veress, K.; Stevens, J.; Dutcher, J. *Phys. Rev. Lett.* **1996**, *77* (10), 2002–2005.
- (69) Kim, J. H.; Jang, J.; Zin, W.-C. *Langmuir* **2001**, *17* (9), 2703–2710.
- (70) Campoy-Quiles, M.; Alonso, M. I.; Bradley, D. D. C.; Richter, L. J. *Adv. Funct. Mater.* **2014**, *24* (15), 2116–2134.
- (71) Campoy-Quiles, M.; Sims, M.; Etchegoin, P. G.; Bradley, D. D. C. *Macromolecules* **2006**, *39* (22), 7673–7680.
- (72) Wang, T.; Pearson, A. J.; Dunbar, A. D. F.; Staniec, P. A.; Watters, D. C.; Coles, D.; Yi, H.; Iraqi, A.; Lidzey, D. G.; Jones, R. A. L. *Eur. Phys. J. E. Soft Matter* **2012**, *35* (12), 129.

- (73) Müller, C.; Andersson, L. M.; Peña-Rodríguez, O.; Garriga, M.; Inganäs, O.; Campoy-Quiles, M. *Macromolecules* **2013**, *46* (18), 7325–7331.
- (74) Liu, D.; Osuna Orozco, R.; Wang, T. *Phys. Rev. E* **2013**, *88* (2), 022601.
- (75) Wang, T.; Pearson, A. J.; Dunbar, A. D. F.; Staniec, P. A.; Watters, D. C.; Yi, H.; Ryan, A. J.; Jones, R. A. L.; Iraqi, A.; Lidzey, D. G. *Adv. Funct. Mater.* **2012**, *22* (7), 1399–1408.
- (76) Langhammer, C.; Larsson, E. M.; Kasemo, B.; Zorić, I. *Nano Lett.* **2010**, *10* (9), 3529–3538.
- (77) Budd, P. M.; Ghanem, B. S.; Makhseed, S.; McKeown, N. B.; Msayib, K. J.; Tattershall, C. E. *Chem. Commun. (Camb)*. **2004**, No. 2, 230–231.
- (78) Budd, P. M.; Elabas, E. S.; Ghanem, B. S.; Makhseed, S.; McKeown, N. B.; Msayib, K. J.; Tattershall, C. E.; Wang, D. *Adv. Mater.* **2004**, *16* (5), 456–459.
- (79) Budd, P. M.; McKeown, N. B.; Fritsch, D. *Macromol. Symp.* **2006**, *245-246* (1), 403–405.
- (80) Robeson, L. M. *J. Memb. Sci.* **2008**, *320* (1-2), 390–400.
- (81) Du, N.; Park, H. B.; Robertson, G. P.; Dal-Cin, M. M.; Visser, T.; Scoles, L.; Guiver, M. D. *Nat. Mater.* **2011**, *10* (5), 372–375.
- (82) Nelson, J. *Mater. Today* **2011**, *14* (10), 462–470.
- (83) Brabec, C. J.; Gowrisanker, S.; Halls, J. J. M.; Laird, D.; Jia, S.; Williams, S. P. *Adv. Mater.* **2010**, *22* (34), 3839–3856.
- (84) Kim, Y.; Yeom, H. R.; Kim, J. Y.; Yang, C. *Energy Environ. Sci.* **2013**, *6* (6), 1909.
- (85) Wang, E.; Hou, L.; Wang, Z.; Hellström, S.; Zhang, F.; Inganäs, O.; Andersson, M. R. *Adv. Mater.* **2010**, *22* (46), 5240–5244.
- (86) Bohren, C. F.; Huffman, D. R. *Absorption and Scattering of Light by Small Particles*; Wiley-VCH: New York, 2007.
- (87) Kreibig, U.; Vollmer, M. *Optical Properties of Metal Clusters*; Springer-Verlag: Berlin Heidelberg, 1995.
- (88) Sönnichsen, C.; Franzl, T.; Wilk, T.; von Plessen, G.; Feldmann, J.; Wilson, O.; Mulvaney, P. *Phys. Rev. Lett.* **2002**, *88* (7), 077402.
- (89) Sönnichsen, C.; Geier, S.; Hecker, N. E.; von Plessen, G.; Feldmann, J.; Ditlbacher, H.; Lamprecht, B.; Krenn, J. R.; Aussenegg, F. R.; Chan, V. Z.-H.; Spatz, J. P.; Möller, M. *Appl. Phys. Lett.* **2000**, *77* (19), 2949.
- (90) Langhammer, C.; Kasemo, B.; Zorić, I. *J. Chem. Phys.* **2007**, *126* (19), 194702.

- (91) Jain, P. K.; Lee, K. S.; El-Sayed, I. H.; El-Sayed, M. A. *J. Phys. Chem. B* **2006**, *110* (14), 7238–7248.
- (92) Meier, M.; Wokaun, A. *Opt. Lett.* **1983**, *8* (11), 581.
- (93) Wokaun, A.; Gordon, J. P.; Liao, P. F. *Phys. Rev. Lett.* **1982**, *48* (14), 957–960.
- (94) Kreibig, U.; Schmitz, B.; Breuer, H. D. *Phys. Rev. B* **1987**, *36* (9), 5027–5030.
- (95) Johnson, P. B.; Christy, R. W. *Phys. Rev. B* **1972**, *6* (12), 4370–4379.
- (96) Langhammer, C.; Yuan, Z.; Zorić, I.; Kasemo, B. *Nano Lett.* **2006**, *6* (4), 833–838.
- (97) Zorić, I.; Zäch, M.; Kasemo, B.; Langhammer, C. *ACS Nano* **2011**, *5* (4), 2535–2546.
- (98) Chen, J.; Albella, P.; Pirzadeh, Z.; Alonso-González, P.; Huth, F.; Bonetti, S.; Bonanni, V.; Åkerman, J.; Nogués, J.; Vavassori, P.; Dmitriev, A.; Aizpurua, J.; Hillenbrand, R. *Small* **2011**, *7* (16), 2341–2347.
- (99) Strohhfeldt, N.; Tittl, A.; Schäferling, M.; Neubrech, F.; Kreibig, U.; Griessen, R.; Giessen, H. *Nano Lett.* **2014**, *14* (3), 1140–1147.
- (100) Schwind, M.; Zhdanov, V. P.; Zorić, I.; Kasemo, B. *Nano Lett.* **2010**, *10* (3), 931–936.
- (101) Schwind, M.; Hosseinpour, S.; Langhammer, C.; Zoric, I.; Leygraf, C.; Kasemo, B. *J. Electrochem. Soc.* **2013**, *160* (10), C487–C492.
- (102) Knight, M. W.; Liu, L.; Wang, Y.; Brown, L.; Mukherjee, S.; King, N. S.; Everitt, H. O.; Nordlander, P.; Halas, N. J. *Nano Lett.* **2012**, *12* (11), 6000–6004.
- (103) Langhammer, C.; Schwind, M.; Kasemo, B.; Zorić, I. *Nano Lett.* **2008**, *8* (5), 1461–1471.
- (104) Link, S.; Wang, Z. L.; El-Sayed, M. A. *J. Phys. Chem. B* **1999**, *103* (18), 3529–3533.
- (105) Zhang, H.; Jin, R.; Mirkin, C. A. *Nano Lett.* **2004**, *4* (8), 1493–1495.
- (106) Mallin, M. P.; Murphy, C. J. *Nano Lett.* **2002**, *2* (11), 1235–1237.
- (107) Wang, G.; Xiao, L.; Huang, B.; Ren, Z.; Tang, X.; Zhuang, L.; Lu, J. *J. Mater. Chem.* **2012**, *22* (31), 15769.
- (108) Cortie, M. B.; McDonagh, A. M. *Chem. Rev.* **2011**, *111* (6), 3713–3735.
- (109) Silkin, V. M.; Chernov, I. P.; Echenique, P. M.; Koroteev, Y. M.; Chulkov, E. V. *Phys. Rev. B* **2007**, *76* (24), 245105.
- (110) Mock, J. J.; Barbic, M.; Smith, D. R.; Schultz, D. A.; Schultz, S. *J. Chem. Phys.* **2002**, *116* (15), 6755.

- (111) Burgin, J.; Liu, M.; Guyot-Sionnest, P. *J. Phys. Chem. C* **2008**, *112* (49), 19279–19282.
- (112) Banholzer, M. J.; Harris, N.; Millstone, J. E.; Schatz, G. C.; Mirkin, C. A. *J. Phys. Chem. C* **2010**, *114* (16), 7521–7526.
- (113) Dahmen, C.; von Plessen, G. *Aust. J. Chem.* **2007**, *60* (7), 447.
- (114) Hu, M.; Chen, J.; Li, Z.-Y.; Au, L.; Hartland, G. V.; Li, X.; Marquez, M.; Xia, Y. *Chem. Soc. Rev.* **2006**, *35* (11), 1084–1094.
- (115) Eustis, S.; el-Sayed, M. A. *Chem. Soc. Rev.* **2006**, *35* (3), 209–217.
- (116) Larsson, E. M. *Nanoplasmonic Sensing - from Biology to Catalysis*, Chalmers University of Technology, 2009.
- (117) Olofsson, L.; Rindzevicius, T.; Pfeiffer, I.; Käll, M.; Höök, F. *Langmuir* **2003**, *19* (24), 10414–10419.
- (118) Morokoshi, S.; Ohhori, K.; Mizukami, K.; Kitano, H. *Langmuir* **2004**, *20* (20), 8897–8902.
- (119) Yonzon, C. R.; Jeoung, E.; Zou, S.; Schatz, G. C.; Mirksich, M.; Van Duyne, R. P. *J. Am. Chem. Soc.* **2004**, *126* (39), 12669–12676.
- (120) Dahlin, A.; Zäch, M.; Rindzevicius, T.; Käll, M.; Sutherland, D. S.; Höök, F. *J. Am. Chem. Soc.* **2005**, *127* (14), 5043–5048.
- (121) Nath, N.; Chilkoti, A. *Anal. Chem.* **2002**, *74* (3), 504–509.
- (122) Haes, A. J.; Hall, W. P.; Chang, L.; Klein, W. L.; Van Duyne, R. P. *Nano Lett.* **2004**, *4* (6), 1029–1034.
- (123) Voller, A.; Bartlett, A.; Bidwell, D. E. *J. Clin. Pathol.* **1978**, *31* (6), 507–520.
- (124) Langhammer, C.; Zorić, I.; Kasemo, B.; Clemens, B. M. *Nano Lett.* **2007**, *7* (10), 3122–3127.
- (125) Dmitriev, A.; Hägglund, C.; Chen, S.; Fredriksson, H.; Pakizeh, T.; Käll, M.; Sutherland, D. S. *Nano Lett.* **2008**, *8* (11), 3893–3898.
- (126) Hao, F.; Nehl, C. L.; Hafner, J. H.; Nordlander, P. *Nano Lett.* **2007**, *7* (3), 729–732.
- (127) Syrenova, S.; Wadell, C.; Nugroho, F. A. A.; Gschneidner, T. A.; Diaz Fernandez, Y. A.; Nalin, G.; Świtlik, D.; Westerlund, F.; Antosiewicz, T. J.; Zhdanov, V. P.; Moth-Poulsen, K.; Langhammer, C. *Nat. Mater.* **2015**, *14* (12), 1236–1244.
- (128) Shegai, T.; Langhammer, C. *Adv. Mater.* **2011**, *23* (38), 4409–4414.
- (129) Liu, N.; Tang, M. L.; Hentschel, M.; Giessen, H.; Alivisatos, A. P. *Nat. Mater.* **2011**, *10* (8), 631–636.

- (130) Larsson, E. M.; Langhammer, C.; Zorić, I.; Kasemo, B. *Science* **2009**, *326* (5956), 1091–1094.
- (131) Larsson, E. M.; Millet, J.; Gustafsson, S.; Skoglundh, M.; Zhdanov, V. P.; Langhammer, C. *ACS Catal.* **2014**, *4* (1), 171–171.
- (132) Wettergren, K.; Schweinberger, F. F.; Deiana, D.; Ridge, C. J.; Crampton, A. S.; Rötzer, M. D.; Hansen, T. W.; Zhdanov, V. P.; Heiz, U.; Langhammer, C. *Nano Lett.* **2014**, *14* (10), 5803–5809.
- (133) Tabib Zadeh Adibi, P.; Mazzotta, F.; Antosiewicz, T. J.; Skoglundh, M.; Grönbeck, H.; Langhammer, C. *ACS Catal.* **2015**, *5* (1), 426–432.
- (134) Gusak, V.; Heiniger, L.-P.; Graetzel, M.; Langhammer, C.; Kasemo, B. *Nano Lett.* **2012**, *12* (5), 2397–2403.
- (135) Fukai, Y. *The Metal-Hydrogen System*; Springer-Verlag, 1993.
- (136) Wadell, C. *Plasmonic Nanostructures for Optical Absorption Engineering and Hydrogen Sensing*, Chalmers University of Technology, 2015.
- (137) Langhammer, C.; Zhdanov, V. P.; Zorić, I.; Kasemo, B. *Chem. Phys. Lett.* **2010**, *488* (1-3), 62–66.
- (138) Sachs, C.; Pundt, A.; Kirchheim, R.; Winter, M.; Reetz, M. T.; Fritsch, D. *Phys. Rev. B* **2001**, *64* (7), 075408.
- (139) Pundt, A.; Sachs, C.; Winter, M.; Reetz, M. T.; Fritsch, D.; Kirchheim, R. *J. Alloys Compd.* **1999**, *293-295*, 480–483.
- (140) Pundt, A.; Suleiman, M.; Bähz, C.; Reetz, M. T.; Kirchheim, R.; Jisrawi, N. M. *Mater. Sci. Eng. B* **2004**, *108* (1-2), 19–23.
- (141) Westerwaal, R. J.; Rooijmans, J. S. A.; Leclercq, L.; Gheorghe, D. G.; Radeva, T.; Mooij, L.; Mak, T.; Polak, L.; Slaman, M.; Dam, B.; Rasing, T. *Int. J. Hydrogen Energy* **2013**, *38* (10), 4201–4212.
- (142) Alefeld, G.; Völkl, J. *Hydrogen in Metals II*; Springer: Berlin Heidelberg, 1978.
- (143) Hughes, R. C.; Schubert, W. K. *J. Appl. Phys.* **1992**, *71* (1), 542.
- (144) Hughes, R. C.; Schubert, W. K.; Zipperian, T. E.; Rodriguez, J. L.; Plut, T. A. *J. Appl. Phys.* **1987**, *62* (3), 1074.
- (145) Wadell, C.; Syrenova, S.; Langhammer, C. *ACS Nano* **2014**, *8* (12), 11925–11940.
- (146) Schlapbach, L.; Züttel, A. *Nature* **2001**, *414* (6861), 353–358.
- (147) Yoshimura, K.; Langhammer, C.; Dam, B. *MRS Bull.* **2013**, *38* (06), 495–503.

- (148) Oumellal, Y.; Rougier, A.; Nazri, G. A.; Tarascon, J.-M.; Aymard, L. *Nat. Mater.* **2008**, *7* (11), 916–921.
- (149) Huiberts, J. N.; Griessen, R.; Rector, J. H.; Wijngaarden, R. J.; Dekker, J. P.; de Groot, D. G.; Koeman, N. J. *Nature* **1996**, *380* (6571), 231–234.
- (150) Manchester, F. D.; San-Martin, A.; Pitre, J. M. *J. Phase Equilibria* **1994**, *15* (1), 62–83.
- (151) Avila, J. I.; Matelon, R. J.; Trabol, R.; Favre, M.; Lederman, D.; Volkmann, U. G.; Cabrera, A. L. *J. Appl. Phys.* **2010**, *107* (2), 023504.
- (152) Tobiška, P.; Hugon, O.; Trouillet, A.; Gagnaire, H. *Sensors Actuators B Chem.* **2001**, *74* (1-3), 168–172.
- (153) Zhao, Z.; Carpenter, M. A.; Xia, H.; Welch, D. *Sensors Actuators B Chem.* **2006**, *113* (1), 532–538.
- (154) Zhao, Z.; Sevryugina, Y.; Carpenter, M. A.; Welch, D.; Xia, H. *Anal. Chem.* **2004**, *76* (21), 6321–6326.
- (155) Fredriksson, H.; Alaverdyan, Y.; Dmitriev, A.; Langhammer, C.; Sutherland, D. S.; Zäch, M.; Kasemo, B. *Adv. Mater.* **2007**, *19* (23), 4297–4302.
- (156) Scriven, L. E. *MRS Proc.* **2011**, *121*, 717.
- (157) Ohring, M. *Materials Science of Thin Films*; Academic Press: USA, 2002.
- (158) Flamm, D. L. *Plasma Processing of Semiconductors*; Dordrecht: The Netherlands, 1997.
- (159) Pięłowski, J.; Gancarz, I.; Staniszevska-Kuś, J.; Paluch, D.; Szymonowicz, M.; Konieczny, A. *Biomaterials* **1994**, *15* (11), 909–916.
- (160) *Plasma Surface Modification of Polymers: Relevance to Adhesion*; Strobel, M., Lyons, C. S., Mittal, K. L., Eds.; VSP: Utrecht, 1994.
- (161) Mattox, D. M. *Handbook of Physical Vapor Deposition (PVD) Processing*; Elsevier: Oxford, 1998.
- (162) Hitchman, M. L.; Jensen, K. F. *Chemical Vapor Deposition Applications*; Academic Press, 1993.
- (163) Syrenova, S.; Wadell, C.; Langhammer, C. *Nano Lett.* **2014**, *14* (5), 2655–2663.
- (164) Frederiksen, M.; Sutherland, D. S. *Nanoscale* **2014**, *6* (2), 731–735.
- (165) Wadell, C.; Nugroho, F. A. A.; Lidström, E.; Iandolo, B.; Wagner, J. B.; Langhammer, C. *Nano Lett.* **2015**, *15* (5), 3563–3570.
- (166) Newton, R. G. *Am. J. Phys.* **1976**, *44* (7), 639.

- (167) Egerton, R. F. *Physical Principles of Electron Microscopy: An Introduction to TEM, SEM, and AEM*; Springer: New York, 2005.
- (168) Betzig, E.; Chichester, R. J. *Science* **1993**, *262* (5138), 1422–1425.
- (169) Grant, A. W.; Hu, Q.-H.; Kasemo, B. *Nanotechnology* **2004**, *15* (9), 1175–1181.
- (170) Moskovits, M.; Srnová-Šloufová, I.; Vlčková, B. *J. Chem. Phys.* **2002**, *116* (23), 10435.
- (171) Rioux, D.; Vallières, S.; Besner, S.; Muñoz, P.; Mazur, E.; Meunier, M. *Adv. Opt. Mater.* **2014**, *2* (2), 176–182.
- (172) Szilágyi, P. Á.; Westerwaal, R. J.; Lansink, M.; van Montfort, H. I.; Trześniewski, B. J.; Garcia, M. V.; Geerlings, H.; Dam, B. *RSC Adv.* **2015**, *5* (108), 89323–89326.
- (173) Li, J.; Ye, J.; Chen, C.; Li, Y.; Verellen, N.; Moshchalkov, V. V.; Lagae, L.; Van Dorpe, P. *ACS Photonics* **2015**, *2* (3), 425–431.

# 9 Appendix

## 9.1 Matlab Program that Extracts Characteristic Plasmonic Readout Parameters Using a Lorentzian Fit

```
function [peak,ex,FWHM] = peakfitlorentz(data,lambda,peak_guess,ran,plotta)
% peakfit: Calculates peak position, centriod position, absorbance at peak,
% and FWHM for spectra measured in absorbance mode.
% Usage:
% [peak, C, ab, FWHM] = peakfit(data,lambda,peak_guess)
% data = matrix of spectra
% lambda = wavelength vector
% peak_guess = guess for peak position
% As default fit-polynom degree is set to 20. For the centroid fit
% span is set to 30 and the range is set to +- 100nm around peak
guess.

%if size(lambda,2)==1
% lambda = lambda';
%end

%if size(data,2)==size(lambda,2)
% data = data';
%end

%[lambda, a] = sort(lambda);
%data = data(a,:);

war = warning('off','MATLAB:polyfit:RepeatedPointsOrRescale'); %stänger av
varningar

data = data./100;
nr = size(data,2);
rangel=peak_guess-ran;
range2=peak_guess+ran;
ranget=[rangel range2];
range=[find(ranget(1)-lambda<0,1,'first'):find(lambda-
ranget(2)<0,1,'last')];

hc = 1.2398e3;
E = hc./lambda(range)';

s = fitoptions('Method','NonlinearLeastSquares',...
'Lower',[0,0,0],...
'Upper',[3,1,5],...
'Startpoint',[1 .5 hc/peak_guess]);
f = fittype('I*(HWHM^2/((x-p)^2+HWHM^2))','options',s);
h = waitbar(0,'Please wait...');

ex = zeros(1,nr);
```

```

peak = zeros(1,nr);
FWHM = zeros(1,nr);
for i = 1:nr
    waitbar(i / nr)
    a = fit(E,data(range,i),f);
    ex(i) = a.I;
    peak(i) = hc./a.p;
    FWHM(i) = hc./(a.p-a.HWHM)-hc./(a.p+a.HWHM);

    if (plotta == 1)&&(i==1)

%plot(lambda(range),data(range,i),lambda(range),a.I*(a.HWHM^2./((hc./lambda
(range)-a.p).^2+a.HWHM^2)))
        plot(lambda,data(:,i),lambda,a.I*(a.HWHM^2./((hc./lambda-
a.p).^2+a.HWHM^2)))
        end

end
close(h)

```